

Chiral model of twisted bilayer graphene realized in a monolayer

Valentin Crépel,¹ Aaron Dunbrack,² Daniele Guerzi,¹ John Bonini,¹ and Jennifer Cano^{1,2}

¹*Center for Computational Quantum Physics, Flatiron Institute, New York, New York 10010, USA*

²*Department of Physics and Astronomy, Stony Brook University, Stony Brook, New York 11794, USA*

We demonstrate that a single layer of graphene subject to a superlattice potential nearly commensurate to a $\sqrt{3} \times \sqrt{3}$ supercell exactly maps to the chiral model of twisted bilayer graphene, albeit with half as many degrees of freedom. We comprehensively review the properties of this “half-chiral model,” including the interacting phases stabilized at integer fillings and the effects of substrate-induced symmetry breaking. We list candidate substrates that could produce a superlattice potential on graphene with the correct periodicity to access the flat band limit. Experimental measurements on a half-chiral moiré heterostructure, in which valley-skyrmions cannot form, could yield insights on the physics they mediate in twisted bilayer graphene.

I. INTRODUCTION

In the five years following its groundbreaking discovery [1, 2], twisted bilayer graphene (TBG) has realized many of the quantum phases thus far discovered in condensed matter physics [3, 4]. Since then, developing an understanding of TBG has been a major area of research, triggering a colossal body of theoretical work aiming at disentangling the physics of this and other moiré materials [5–20].

In this quest, a particularly simple yet powerful and predictive approach was the introduction of an analytically tractable model — dubbed the chiral model [5] — obtained by slight simplification from earlier continuum models of TBG [6, 7, 21]. The chiral model captures the essence of correlation in TBG in that it features eight-fold degenerate *exact* flat bands for certain magic values of the twist angle [8]. Mathematically, the perfect degeneracy of these bands stems from an emergent chiral symmetry which is only weakly broken in TBG [5, 10], making the chiral model a good qualitative guide to appreciate the physics of TBG while making analytical progress. For instance, the chiral symmetry provides an intuitive explanation for the insulating states at integer filling by analogy with quantum Hall ferromagnetism, which helps rationalize the quantum anomalous Hall (QAH) state at filling $n = 3$ in TBG [22–26]. The analogy to Hall systems also hints at the potential role of skyrmions as bosonic glue in TBG’s superconducting state [27–29]. Finally, the chiral flat bands can be formally written as elements of a Landau level [30–32], allowing for the definition of exact multi-component fractional Chern insulators [33–36] which may describe those measured in TBG at finite field [37].

It remains an open question which aspects of the chiral model can be smoothly transferred to TBG. Answering this question turns out to be as computationally challenging as the direct simulation of the continuum model for TBG [13, 38, 39]. As an alternate path forward, we propound the design of novel moiré materials which exactly realize the chiral model. If such a material existed, comparison of its phase diagram with that of TBG would elucidate which phases of the latter are smoothly con-

nected to the chiral model. Even more interesting, theoretical questions concerning which physics can be directly attributed to valley-skyrmions in TBG become similarly addressable through a moiré analog of the chiral model with half as many degrees of freedom — the “half-chiral model” — in which such skyrmions cannot form.

To this end, we describe an exact realization of the half-chiral model from a superlattice potential nearly commensurate to a $\sqrt{3} \times \sqrt{3}$ supercell of graphene — dubbed a near- $\sqrt{3}$ matched potential hereafter — imposed onto a graphene monolayer. Since this potential varies on a scale comparable to graphene’s lattice constant, it cannot be engineered by either twist or strain, but can be produced by electrostatic coupling to a substrate. Far from a theoretic abstraction, Ref. [40] presented a similar analysis motivated by their experimental data on a SiC/graphene heterostructure, noting the relation to the half-chiral model for large values of the graphene-substrate coupling.

In the present manuscript, we provide a complete picture for the realization of the half-chiral model using a near- $\sqrt{3}$ matched substrate-induced potential. We introduce the model in Sec. II. In Sec. III we consider the effect of interactions and show that the many body ground states at integer filling can realize QAH states similar to chiral TBG. In Sec. IV, we provide a list of candidate substrates together with their most important symmetry breaking effects. Our work paves the way for more proposals and designs of moiré materials capable of answering questions about the many-body physics of TBG, whose full phase diagram remains out of current numerical reach.

II. HALF-CHIRAL MODEL

In this section, we model the graphene-substrate heterostructure described in the introduction, in which a substrate provides a near- $\sqrt{3}$ matched electrostatic potential that directly couples the two valleys of graphene on an emergent moiré scale.

We assume the potential is onsite and hence diagonal in the sublattice index. It maps exactly to a term that

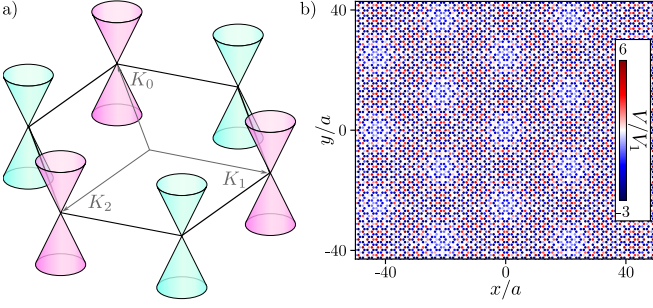


FIG. 1. a) The two valleys of graphene are coupled by a near- $\sqrt{3}$ matched potential with reciprocal lattice vectors $(1 + \epsilon)K_{0,1,2}$, which forms a moiré pattern when evaluated on graphene sites, as shown in (b) for $\epsilon = 0.07$.

was shown in Ref. [41] to allow for a vanishing Dirac cone velocity. If the moiré coupling furthermore respects the original rotation, mirror, and time reversal symmetries of the monolayer, the vanishing Dirac cone velocity implies the existence of perfectly flat bands [42]. A related model in which the potential is not diagonal in sublattice has been studied in Ref. [43].

A. Setup

The low-energy physics of a graphene monolayer derives from its K and K' points, described by the effective continuum Hamiltonians

$$H_K(\bar{k}) = -v\bar{k} \times \tau, \quad H_{K'}(\bar{k}) = v\bar{k} \times \tau^*, \quad (1)$$

with \bar{k} the deviation from the K/K' points, τ the sublattice Pauli matrices, and v the Fermi velocity of graphene. Here, we use the convention $e_{\pm} = (3/2, \pm\sqrt{3}/2)$ for the Bravais lattice vectors, $r_A = (1, 0)$ and $r_B = (1/2, \sqrt{3}/2)$ for the position of orbitals in the unit cell, and have set graphene's lattice constant as the unit of length. This choice centers the two valleys around the $\tau_z K_{n=0,1,2}$ corners of the Brillouin zone (BZ), where

$$K_n = K \left(\sin \frac{2n\pi}{3}, \cos \frac{2n\pi}{3} \right), \quad K = \frac{4\pi}{3\sqrt{3}}. \quad (2)$$

The two valleys are coupled by a near- $\sqrt{3}$ matched onsite potential of the form

$$V(r) = 2V_1 \sum_{n=0}^2 \cos[(K_n + q_n) \cdot r], \quad q_n = \epsilon K_n \quad (3)$$

with $|\epsilon| \ll 1$ (see Fig. 1a). For $\epsilon = 0$, the potential folds the $\pm K_n$ onto the Γ point of graphene's BZ and enlarges the unit cell to $\sqrt{3} \times \sqrt{3}$. However, in this case, the form of Eq. (3) shows that $V(r)$ identically vanishes on all graphene sites. For nonzero but small ϵ , this potential forms a moiré pattern with lattice constant $a_m = \epsilon^{-1}$ due to the small mismatch q_n between the reciprocal lattice

| Symmetry | Original | TBG _K | Chiral | k_x | k_y | r_x | r_y |
|----------------------------------|------------------------|-------------------------|-------------------------|-------|-------|-------|-------|
| C_{2x} | $i\sigma_x\mu_x$ | $i\tau_x\sigma_x\mu_x$ | $i\tau_x\sigma_x\mu_x$ | + | − | + | − |
| C_{2y} | $i\tau_x\sigma_y$ | $-i\tau_y\sigma_y\mu_z$ | $-i\tau_z\sigma_y\mu_y$ | − | + | − | + |
| C_{2z} | $i\tau_x\sigma_z\mu_x$ | $-i\tau_z\sigma_z\mu_y$ | $-i\tau_y\sigma_z\mu_z$ | − | − | − | − |
| I | $\tau_x\mu_x$ | $-\tau_z\mu_y$ | $-\tau_y\mu_z$ | − | − | − | − |
| T | $i\sigma_y\mu_x K$ | $\tau_y\sigma_y\mu_y K$ | $\tau_y\sigma_y\mu_y K$ | − | − | + | + |
| SU(2) _{Spin} | $\sigma_{x,y,z}$ | $\sigma_{x,y,z}$ | $\sigma_{x,y,z}$ | + | + | + | + |
| Λ_z | $\tau_z\mu_z$ | τ_z | μ_z | + | + | + | + |
| $\Lambda_x = i\sigma_x C_{2z} T$ | $\tau_x K$ | $\tau_x K$ | $\mu_x K$ | + | + | − | − |

TABLE I. Symmetries of the model represented in the original [Eq. (4)], TBG_K [Eq. (5)] and chiral [Eq. (8)] bases, with the exact symmetries of graphene (crystalline and time-reversal) given above the second double-line. The last four columns indicate whether the symmetry changes the sign of each component of momentum and position. Λ_z anticommutes with the Hamiltonian, while all other symmetries commute with it. In the original basis, τ , σ and μ are sublattice, spin and valley Pauli matrices, respectively. Identity matrices τ_0 , σ_0 , μ_0 are left implicit.

vectors of the potential and the edges of the graphene Brillouin zone [44], as shown in Fig. 1b.

The effective Hamiltonian of this moiré system is obtained by projecting $V(r)$ near the K/K' points, yielding

$$H^0 = \begin{bmatrix} H_K & \tilde{V}(r) \\ \tilde{V}(r)^\dagger & H_{K'} \end{bmatrix}, \quad \tilde{V}(r) = V_1 \sum_{n=0}^2 e^{i(q_n \cdot r + n\phi\tau_z)}, \quad (4)$$

where $\phi = 2\pi/3$. The phases in \tilde{V} are set by $K_n \cdot (r_A - r_B) = 2n\phi \pmod{2\pi}$ (see Appendix A for details). This model preserves the crystalline and time-reversal symmetries of graphene. Reintroducing the spin, implicit in Eq. (4), H^0 is also invariant under SU(2) spin rotations, implemented by the σ Pauli matrices, and under products such as $\Lambda_x = i\sigma_x C_{2z} T$, which can be understood as a spinless version of $C_{2z} T$. These symmetries are summarized in Table I, which also lists a more subtle anticommuting symmetry, Λ_z , whose properties and consequences will be studied shortly.

B. Mapping to chiral model

We now map the Hamiltonian in Eq. (4) onto the chiral model for the K valley of TBG by a series of unitary transformations. We first make a gauge choice for the A and B orbitals of each valley with $\mathcal{U}_1 = e^{i\pi\tau_z\mu_z/4}$, where μ are valley Pauli matrices. Then, we rotate the sublattice basis in K' so that both valleys feature the same helicity using $\mathcal{U}_2 = \text{diag}(\tau_0, \tau_y)$. The resulting Hamiltonian is

$$H^{\text{TBG}_K} = (\mathcal{U}_1 \mathcal{U}_2)^\dagger H^0 (\mathcal{U}_1 \mathcal{U}_2) = \begin{bmatrix} v\bar{k} \cdot \tau & T(r) \\ T(r)^\dagger & v\bar{k} \cdot \tau \end{bmatrix}, \quad (5)$$

with

$$T(r) = V_1 \sum_n e^{iq_n \cdot r} [(\hat{q}_n \times \tau) \cdot \hat{z}], \quad (6)$$

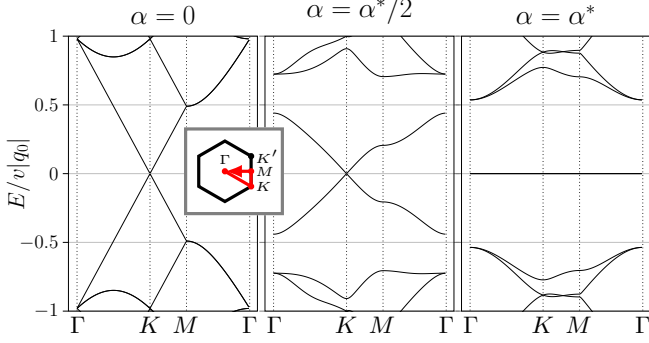


FIG. 2. Band structure of the continuum model Eq. (4) plotted along the high-symmetry path of the moiré mini-Brillouin zone illustrated in the inset. The bandwidth of the band closest to charge neutrality exactly vanishes when the coupling strength $\alpha = V_1/|vq_0|$ reaches the value $\alpha^* \simeq 0.586$.

with \hat{q}_n the direction of q_n . This is precisely the form obtained in the K valley of twisted bilayer graphene in absence of AA and BB couplings [6, 7], hence the super-script TBG_K.

All terms in Eq. (5) are purely off diagonal in the sublattice index. To make this block structure more explicit, we introduce one last unitary transformation

$$H^{\text{chiral}} = \mathcal{U}_3^\dagger H^{\text{TBG}_K} \mathcal{U}_3, \quad \mathcal{U}_3 = \begin{bmatrix} 1 & 0 & 0 & 0 \\ 0 & 0 & 1 & 0 \\ 0 & 1 & 0 & 0 \\ 0 & 0 & 0 & 1 \end{bmatrix}, \quad (7)$$

which, as promised, maps our system to the chiral model for the K valley of TBG [5]

$$H^{\text{chiral}} = v|q_0| \begin{bmatrix} 0 & D \\ D^\dagger & 0 \end{bmatrix}, \quad D = \begin{bmatrix} -2i\partial_z & \alpha U(r) \\ \alpha U(-r) & -2i\partial_z \end{bmatrix}, \quad (8)$$

with $\partial_z = (\partial_x + i\partial_y)/|q_0|$ and

$$U(r) = \sum_n e^{i(q_n \cdot r - n\phi)}, \quad \alpha = \frac{V_1}{v|q_0|}. \quad (9)$$

For convenience, we summarize the action of the successive unitary transformations on the original basis

$$(\mathcal{U}_1 \mathcal{U}_2 \mathcal{U}_3)^\dagger \begin{bmatrix} (A, K) \\ (B, K) \\ (A, K') \\ (B, K') \end{bmatrix} = e^{-i\pi/4} \begin{bmatrix} (A, K) \\ -i(B, K') \\ i(B, K) \\ -(A, K') \end{bmatrix}. \quad (10)$$

Up to an orbital-valley dependent gauge choice, this transformation sorts the lattice degrees of freedom with respect to their chirality, *i.e.*, the periodic part of the Bloch orbitals projected on A near K and B near K' exhibit the same phase winding around the origin, which is opposite to the winding for (B, K) and (A, K') [45, 46]. These two sectors are distinguished by the chiral operator, which takes the form $\Lambda_z = \tau_z \mu_z$ in the original basis (see Table I).

| spinless chiral TBG | | C_{2z} | $i\sigma_y T$ | Λ_x |
|---------------------|------------------------------|------------|---------------|-------------|
| $C = 1$ | $(A1, A2) \quad K$ | \rangle | \rangle | \rangle |
| | $(B1, B2) \quad K'$ | | | |
| $C = -1$ | $(B1, B2) \quad K$ | \rangle | \rangle | \rangle |
| | $(A1, A2) \quad K'$ | | | |
| half-chiral model | | σ_x | T | Λ_x |
| $C = 1$ | $(AK, BK') \quad \uparrow$ | \rangle | \rangle | \rangle |
| | $(AK, BK') \quad \downarrow$ | | | |
| $C = -1$ | $(AK', BK) \quad \uparrow$ | \rangle | \rangle | \rangle |
| | $(AK', BK) \quad \downarrow$ | | | |

FIG. 3. Flat bands in the spinless chiral model of TBG (top) [5, 38] and in the half-chiral model (bottom), gathered by Chern number, or chirality. In the former, Pn indicates the $P = A/B$ orbital in layer n . Symmetries relating the different bands are depicted on the right, showing how spin in our model plays a role equivalent to valley in spinless chiral TBG.

C. Flat bands and degeneracy

In the chiral model of twisted bilayer graphene, perfectly flat bands arise when the twist angle and interlayer hopping strength are tuned so that α – the only dimensionless parameter of the theory – belongs to a particular set of values (0.586, 2.221, 3.75, ...) [5]. The direct mapping to Eq. (8) ensures that our model also enjoys perfectly flat bands when the ratio $\alpha = V_1/(v|q_0|)$ takes values in that set. In the following we employ α^* to denote the lowest of these magic values. Equivalently, V_1^* is the magic amplitude of the potential for a given wavevector $|q_0|$. As an illustration, we plot in Fig. 2 the band structure of the the moiré Hamiltonian in Eq. (4) for different values of α between 0 and the first magic value $\alpha^* \simeq 0.586$.

Fig. 2 shows that our model features two spin-degenerate flat bands at $\alpha = \alpha^*$. One of these flat bands is annihilated by D and lives in the first chirality block $\{AK, BK'\}$, while the other – its time-reversed and particle-hole partner – is an exact zero mode of D^\dagger and lives in the opposite chirality block $\{BK, AK'\}$. We label them by their corresponding chiral operator eigenvalue Λ_z , *i.e.* by + and –, respectively. Finally, the flat bands inherit a non-zero Chern number $C(\Lambda_z) = \Lambda_z$ from the winding of their constituting orbitals [47, 48]. Since the bands in opposite chirality sectors are time-reversal partners, they must have opposite Chern number.

An important distinction between our model and the chiral model of TBG is the number of flat bands. In the chiral limit of TBG, there are $2^3 = 8$ flat bands, labelled by spin, valley, and sublattice. In contrast, our system only displays $2^2 = 4$ flat bands at the magic point, labelled by spin and sublattice-valley chirality. Thus, we have provided a realization of the half-chiral model. In spite of this lower degeneracy, we can draw some analogy between the half-chiral model and the spinless model for TBG by looking at how symmetries of the two models couple the different flat bands, as summarized in Fig. 3.

There, we observe that spin in our model plays a role analogous to the valley index in spinless chiral TBG.

III. INTERACTIONS AT INTEGER FILLING

We now consider the effect of symmetry-preserving interaction terms on the Hamiltonian in Eq. (4) in the chiral limit. In Sec. III A, we show how symmetry constrains the form factors of the interaction. Using these considerations, in Sec. III B we derive the many body ground states at integer filling. The discussion proceeds similarly to chiral TBG, accounting for the lower internal degeneracy of our model. Finally, we highlight the robustness of the Chern insulators obtained when an odd number of the flat bands are filled.

A. Form factors

Let us first show that the form factors of the interaction are diagonal in the σ_z and Λ_z indices using the SU(2) spin rotation and chiral symmetry of our model. We further relate these diagonal form factors using the σ_x and Λ_x symmetries.

Consider an inter-particle repulsive potential with Fourier transform $U_q > 0$. After projection to the flat band subspace, electronic interactions take the form

$$H_I = \int dq U_q \rho_q \rho_{-q}, \quad \rho_q = \sum_{k,\alpha,\beta} c_{\alpha,k}^\dagger \langle \psi_{k,\alpha} | \psi_{k+q,\beta} \rangle c_{\beta,k+q}, \quad (11)$$

where $\alpha = (\sigma, \gamma)$ labels the bands using their spin and chirality indices, while $c_{\alpha,k}$ and $|\psi_{k,\alpha}\rangle$ respectively correspond to the fermionic operator and the periodic Bloch wavefunction of the electronic mode in band α with momentum k .

Since each band has a well-defined chirality and spin, the form factors $\langle \psi_{k,\alpha} | \psi_{k+q,\beta} \rangle$ appearing in the projected density ρ_q drastically simplify. Specifically, using the identities $\Lambda_z^2 = \sigma_z^2 = 1$, we obtain

$$\begin{aligned} \langle \psi_{(\sigma',\gamma')} | \psi_{(\sigma,\gamma)} \rangle & \quad (12) \\ &= \langle \psi_{(\sigma',\gamma')} | \Lambda_z^2 | \psi_{(\sigma,\gamma)} \rangle = \gamma\gamma' \langle \psi_{(\sigma',\gamma')} | \psi_{(\sigma,\gamma)} \rangle \\ &= \langle \psi_{(\sigma',\gamma')} | \sigma_z^2 | \psi_{(\sigma,\gamma)} \rangle = \sigma\sigma' \langle \psi_{(\sigma',\gamma')} | \psi_{(\sigma,\gamma)} \rangle, \end{aligned}$$

which proves that $\langle \psi_{(\sigma',\gamma')} | \psi_{(\sigma,\gamma)} \rangle = 0$ when $\gamma \neq \gamma'$ or $\sigma \neq \sigma'$. The projected density operator thus assumes the diagonal form

$$\rho_q = \sum_{k,\alpha} F_{k,q}^\alpha c_{\alpha,k}^\dagger c_{\alpha,k+q}, \quad F_{k,q}^\alpha = \langle \psi_{k,\alpha} | \psi_{k+q,\alpha} \rangle. \quad (13)$$

Additional progress can be made by exploiting the full spin symmetry of the model using σ_x and the emergent Λ_x symmetry (see Table I), which also both square to the

identity

$$\begin{aligned} F_{k,q}^{(\uparrow,\gamma)} &= \langle \psi_{(\uparrow,\gamma)} | \sigma_x^2 | \psi_{(\uparrow,\gamma)} \rangle = \langle \psi_{(\downarrow,\gamma)} | \psi_{(\downarrow,\gamma)} \rangle = F_{k,q}^{(\downarrow,\gamma)}, \\ F_{k,q}^{(\sigma,+)} &= \langle \psi_{(\sigma,+)} | \Lambda_x^2 | \psi_{(\sigma,+)} \rangle = \langle \psi_{(\sigma,-)}^* | \psi_{(\sigma,-)}^* \rangle = [F_{k,q}^{(\sigma,-)}]^*, \end{aligned} \quad (14)$$

where the complex conjugation in the second line come from the anti-unitarity of Λ_x . This fixes

$$F_{k,q}^{(\sigma,\gamma)} = F_{k,q} e^{i\Phi_{k,q}\gamma}, \quad (15)$$

for some real functions $F_{k,q}$ and $\Phi_{k,q}$, similarly to the result obtained in the chiral model describing a single valley of TBG [38]. It follows that our half-chiral model has the same $U(2) \times U(2)$ symmetry as the spinless chiral model of TBG (see Fig. 3).

Note that it is not possible to gauge away the phase $\Phi_{k,q}$ because of the non-zero Chern number of the chiral bands. Indeed, noticing that the Berry connection can be written as $\mathcal{A}_k^{(\sigma,\gamma)} = \text{Im}(\nabla_q F_{k,q}^{(\sigma,\gamma)})_{q=0} = \gamma(\nabla_q \Phi_{k,q})_{q=0}$, we must have

$$\sum_k [(\partial_{k_x} \partial_{q_y} - \partial_{k_y} \partial_{q_x}) \Phi_{k,q}]_{q=0} = 2\pi. \quad (16)$$

This ensures that $F_{k,q}^{(\sigma,+)} \neq F_{k,q}^{(\sigma',-)}$ at least at one point in the Brillouin zone. Thus, Eq. (15) cannot be further simplified.

B. Integer fillings

Equipped with the form factors in Eq. (15), we now investigate how interactions lift the extensive degeneracy of the flat band subspace at integer fillings using arguments borrowed from quantum Hall ferromagnetism [49, 50]. Our analysis relies on two facts: (i) the interacting Hamiltonian is positive, *i.e.* for any many body state $|\Psi\rangle$, $\langle \Psi | H_I | \Psi \rangle = \int dq U_q ||\rho_{-q}|\Psi\rangle||^2 \geq 0$; and (ii) any state in which each of the chiral bands is either filled or empty is annihilated by ρ_q for all q . Since the states described in (ii) have no interaction energy, and no kinetic energy by virtue of the flat bands, they are necessarily ground states following (i). Any other state will acquire some interaction energy from one of the ρ_q . This energy, though possibly infinitesimal (*e.g.* for magnons), ensures that the ground state is a band ferromagnet in the chiral basis.

We now discuss each integer filling in turn.

a. At $n = \pm 2$, the four bands at zero energy are either all fully filled or all empty. The total Chern number of the occupied band is zero and all spin components are equally occupied. The system is a topologically-trivial band insulator.

b. At $n = \pm 1$, an odd number of α bands must be filled, following (i) and (ii) above. The ground state therefore carries a non-trivial Chern number, which manifests in an quantum anomalous Hall effect and a spontaneous spin-polarization.

c. *At $n = 0$,* our prescription for filling two of the four flat bands gives six degenerate ground states with sharply different physical properties. Some are paramagnetic with a total Chern number $|C_{\text{tot}}| = 2$, some are spin polarized with $|C_{\text{tot}}| = 0$, and others are paramagnetic and carry no total Chern number. To predict the behavior at charge neutrality, we exploit a hierarchy between the various symmetries of our model (see Table I). The crystalline symmetries are protected by the carbon links of graphene, while the Λ_z symmetry is an emergent symmetry, which we can realistically assume is more fragile. Provided interaction scales remain stronger than kinetic ones, the weak breaking of Λ_z only changes the form factors, which remain spin-diagonal but acquire non-zero off-diagonal coefficients between Bloch state of opposite chiralities. In this situation, the many-body states with vanishing interaction energy must have all bands that are mixed by a form factor either entirely empty or fully filled. This lifts the previous six-fold degeneracy and results in a spin-polarized ground state with $|C_{\text{tot}}| = 0$, where two flat bands with opposite chirality and equal spin are completely occupied.

C. Chern insulator robustness

At the magic angle and for $n = \pm 1$, we have just seen that the half-chiral model spontaneously breaks time-reversal symmetry and exhibits a quantized anomalous Hall effect. To determine the robustness of this state we now study the spectra of charged and neutral excitations, both at and away from the magic value of α^* .

Figs. 4a-b show the spectra of charge- e excitations above the ground state polarized along $\alpha = (\downarrow, -)$ at $n = -1$ (details in Appendix B). The charge sector remains gapped over a rather large range of α around the magic point, which ensures quantization of the transverse conductance at low temperature and the dissipationless flow of edge current [51].

The neutral excitation spectrum, shown in Figs. 4c-d, contains a gapless magnon branch resulting from the spontaneously broken continuous $\text{SU}(2)$ spin symmetry; this mode disperses quadratically [52, 53]. In addition, the broken discrete \mathbb{Z}_2 chiral symmetry yields a branch of gapped excitations with chirality opposite to that of the ground state. We identify these states using a flavor-flip analysis (see Appendix C).

For $\alpha < \alpha^*$, the particle-hole dispersion softens the magnon spectrum near the κ_{\pm} points, while the charge gap decreases. At a critical value of α , which depends on the global interaction scale, excitations from both spectra fall below zero energy, which makes the ferromagnetic state unstable. The position of the collapse for the charge- e spectrum is well captured by a Stoner-like criterion: it roughly occurs when the mean kinetic energy $\pm|W|$ of the bands near charge neutrality (Fig. 2) equals the charge gap obtained at $\alpha = \alpha^*$. Using the parameters in Fig. 4 as an illustration, the charge gap

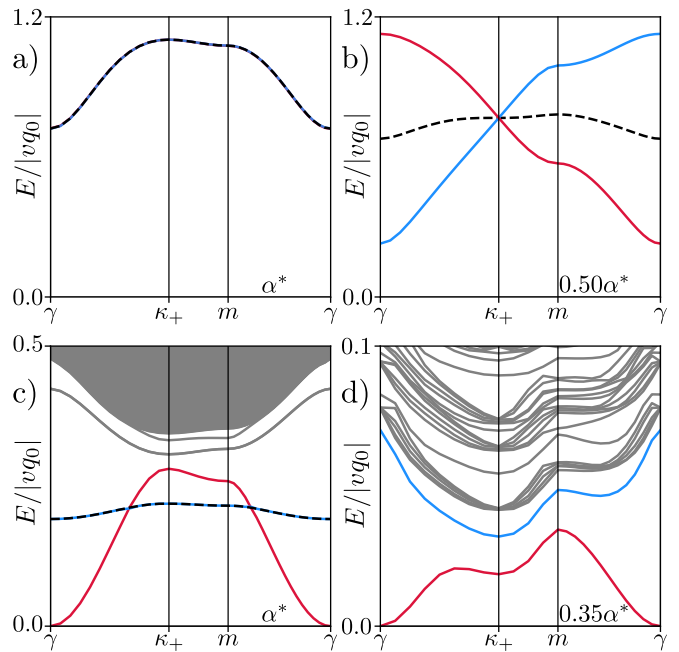


FIG. 4. (a-b) Charged and (c-d) neutral excitation spectrum above the state fully polarized along $\alpha = (\downarrow, -)$ at filling $n = -1$, at (a,c) and away from (b,d) the magic point. Charged excitation spectra (a,b) remain gapped over a wide region around α^* , granting topological protection to the Chern insulator. The neutral excitation spectrum features a gapless magnon (red) and spin-degenerate gapped modes (blue, black) expected from the spontaneously broken $\text{SU}(2)$ spin and \mathbb{Z}_2 chiral symmetries, respectively.

is equal to $\simeq 0.7|vq_0|$ at the magic point, and it closes when $W = 0.66|vq_0|$, which corresponds to $\alpha \simeq 0.3\alpha^*$. Despite its smaller gap at κ_+ when $\alpha = \alpha^*$, the magnon spectrum closes at nearly the same value of $\alpha \simeq 0.32\alpha^*$.

The phenomenology of these excitations reproduce that obtained in the chiral model for TBG [8–13], which is expected from the exact mapping presented in Sec. II B. Naturally, excitations above other insulating states, for instance the one stabilized at $n = 0$ filling, can similarly be obtained. The only difference between TBG and the system studied here is the lower number of flavor-flip excitations available in the half-chiral model. As a result, some of the gapless excitations identified in TBG, such as valley-skyrmions, do not appear in our model.

IV. MATERIAL REALIZATION

We now discuss how to impose the periodic potential in Eq. (3) on graphene. Since the potential varies on a microscopic scale, it is unlikely to be realized by artificial patterning [54–56], which provides a valuable tuning knob for designer flat bands with a larger periodicity [18, 57–61]. Instead, inspired by recent experiments on SiC/graphene heterostructures [40], we propose to realize the model in a heterostructure where graphene

sits on a substrate nearly lattice-matched to a $\sqrt{3} \times \sqrt{3}$ graphene supercell. In Sec. IV A we propose candidate materials to realize this situation.

In such a setup, the potential on graphene will generally contain additional terms beyond the leading harmonic of the chiral-symmetric model in Eq. (3). Sec. IV B is devoted to considering such terms. First, in Sec. IV B 1, we consider terms that break the chiral symmetry but preserve the crystalline symmetries of graphene. In presence of these terms, magic values of V_1 where the Fermi velocity vanishes still exist, but do not necessarily feature perfect flat bands. Then, in Sec. IV B 2, motivated by the material candidates in Table II, we consider additional perturbations breaking some rotational and mirror symmetries of the half-chiral model.

A. Candidate substrates

In Table II and Appendix E we list candidate substrates whose surface periodicity nearly matches the $\sqrt{3} \times \sqrt{3}$ graphene supercell. As our proposed half-chiral model breaks translation symmetry in monolayer graphene via a potential term, but does not have inter-layer hopping, we require candidate substrates to possess a sizeable band gap (> 1 eV). Table II lists candidates predicted to be thermodynamically stable [62, 63] whose surface lattice vectors are near 2% mismatch from the $\sqrt{3} \times \sqrt{3}$ graphene supercell.

The candidate substrates were identified from a pool of 2013 systems using the Materials Project API [64, 65] to filter for those with reported experimental data, a band gap greater than 1 eV, and fewer than 10 sites per unit cell. Following the lattice matching procedure of Ref. [66], 90 candidate substrates were identified with hexagonal surface periodicity nearly matching the $\sqrt{3} \times \sqrt{3}$ graphene supercell. The 65 thermodynamically stable systems are listed in Table II and Table IV of Appendix E. Those in Table II have a computed lattice mismatch of 1.5-2.5%, yielding a moiré length scale similar to that of magic angle TBG. The remaining 25 candidates in Table V are predicted to lie above the convex hull of the zero temperature Gibbs free energy and thus are metastable or only stable under particular conditions such as high pressure. These systems and their energies above the convex hull are tabulated in Table V of Appendix E.

The candidates we propose meet some necessary, but not sufficient, conditions for a physical realization of the emergent flat bands in the half-chiral model. They thus provide a good starting point for future theoretical and experimental investigation.

One of many factors to determine whether graphene on a particular substrate realizes the half chiral model is the physical potential induced by that substrate. For each candidate, we have used the lattice mismatch ϵ to find $V_1^* = \alpha^* v \epsilon |K_0|$, shown in Table II. In practice, the full potential has a particular value of the first harmonic V_1 ,

as well as higher harmonics. Their magnitudes depend on the particular termination of the substrate and on the relaxation of both graphene and the substrate surface. Tuning this potential via, for instance, substrate strain, may provide a viable path toward engineering flat bands.

B. Substrate-induced symmetry breaking

The potential induced on graphene from proximity to a substrate with a $\sqrt{3} \times \sqrt{3}$ supercell will generally contain additional terms beyond those in Eq. (3). As in Ref. [43], we expand them as a function of reciprocal lattice vectors of the substrate. Projected into the low-energy basis given in Eq. (5) (TBG_K column in Table I), the most general Hamiltonian for the graphene layer compatible with the moiré periodicity is a sum of harmonics

$$H_{\text{eff}} = \left[\sum_G H_{G,+} e^{iG \cdot r} \quad \sum_Q H_Q e^{iQ \cdot r} \right] \quad (17)$$

where G runs over the moiré reciprocal lattice vectors and Q runs over $G + q_0$. Eq. (17) simplifies to the half-chiral model in Eq. (4) when all sums are restricted to the lowest symmetry-related set of harmonics with $H_{G=0,\pm}$ the $k \cdot p$ Hamiltonian of graphene close to the $\pm K$ valley, and $H_{q_{0,1,2}}$ reproducing $T(r)$ in Eq. (6).

We now consider the leading corrections beyond the half-chiral limit. We work to zeroth order in k , aside from $H_{G,\pm}$ for $G = 0$, which is computed to first order in k . Specifically, we first assume that crystal symmetries are preserved, but break chiral symmetry. We then characterize the behavior of the magic coupling, defined as the coupling for which the Fermi velocity vanishes, and the bandwidth at that coupling. Finally, since many of the substrates in Table II break the rotational symmetry of graphene, we consider corresponding symmetry-breaking terms. The derivation of the symmetry-breaking terms from symmetry considerations is performed in Appendix D.

1. Breaking chiral symmetry

To linear order in k , the most general form of the zeroth harmonic, $H_{0,\pm}$ allowed by crystal symmetry is

$$H_{0,\pm} = \mu + v k \cdot \tau, \quad (18)$$

which differs from Eq. (5) by a renormalized Fermi velocity and an overall chemical potential, setting the scale and zero of energy, respectively. The latter can be physically tuned by electrostatic gating.

New terms arise from the off-diagonal coupling H_Q in Eq. (17). The first and third harmonics, with $Q_i = \epsilon K_i$ and $Q_i = -2\epsilon K_i$, respectively, are constrained by crystal symmetry to the form

$$H_Q = V_n (\hat{Q} \times \tau) \cdot \hat{z} + i t_n \tau_z, \quad (19)$$

| Composition | mp-id | Surface | Lattice | SG | $ \epsilon \%$ | V_1^* (meV) | Moiré length (nm) | Gap (eV) |
|------------------------------------|---------|---------|---------|----------|----------------|---------------|-------------------|----------|
| CdS | 672 | 001 | hex. | $P6_3mc$ | 1.56 | 102 | 15.84 | 1.12 |
| CsLaS ₂ | 561586 | 111 | rhomb. | $R3m$ | 1.59 | 104 | 15.54 | 2.59 |
| TbTiSe ₂ | 569507 | 111 | rhomb. | $R3m$ | 1.61 | 106 | 15.28 | 1.45 |
| Ba ₂ CuBrO ₂ | 552934 | 111 | rhomb. | $R3m$ | 1.62 | 106 | 15.23 | 2.33 |
| BaHgO ₂ | 3915 | 111 | rhomb. | $R3m$ | 1.65 | 108 | 14.95 | 2.37 |
| NaGdSe ₂ | 999489 | 111 | rhomb. | $R3m$ | 1.69 | 111 | 14.60 | 1.63 |
| CsSmS ₂ | 9082 | 111 | rhomb. | $R3m$ | 1.71 | 113 | 14.41 | 2.24 |
| Ba ₂ BrN | 1018098 | 111 | rhomb. | $R3m$ | 1.80 | 118 | 13.74 | 1.31 |
| YTiSe ₂ | 1067744 | 111 | rhomb. | $R3m$ | 1.88 | 124 | 13.11 | 1.45 |
| PrTiSe ₂ | 999289 | 111 | rhomb. | $R3m$ | 1.89 | 124 | 13.06 | 1.45 |
| RbBiS ₂ | 30041 | 111 | rhomb. | $R3m$ | 1.92 | 126 | 12.89 | 1.37 |
| DyTiSe ₂ | 568062 | 111 | rhomb. | $R3m$ | 1.98 | 130 | 12.44 | 1.43 |
| NdTiS ₂ | 3664 | 111 | rhomb. | $R3m$ | 1.99 | 131 | 12.42 | 1.74 |
| YbSe | 286 | 111 | cubic | $Fm3m$ | 2.08 | 136 | 11.89 | 2.03 |
| SrHfClO | 24066 | 001 | hex. | $P6_3mc$ | 2.09 | 137 | 11.82 | 4.98 |
| HoTiSe ₂ | 569178 | 111 | rhomb. | $R3m$ | 2.16 | 142 | 11.43 | 1.42 |
| ZnTe | 2176 | 111 | cubic | $F43m$ | 2.28 | 150 | 10.83 | 1.08 |
| NaTbSe ₂ | 999127 | 111 | rhomb. | $R3m$ | 2.35 | 154 | 10.52 | 1.90 |
| RbLuSe ₂ | 10785 | 111 | rhomb. | $R3m$ | 2.42 | 159 | 10.21 | 2.11 |
| TiCoSb | 5967 | 111 | cubic | $F43m$ | 2.42 | 159 | 10.20 | 1.07 |
| Ca(MgAs) ₂ | 9564 | 001 | hex. | $P3m1$ | 2.46 | 162 | 10.02 | 1.26 |
| MnI ₂ | 28013 | 001 | hex. | $P3m1$ | 2.49 | 163 | 9.93 | 1.18 |

TABLE II. Thermodynamically stable candidate substrates with $1.5\% < |\epsilon| < 2.5\%$. Additional candidates are given in Appendix E. The columns, from left to right, indicate the stoichiometry of the substrate, the database ID (with hyperlink) of the corresponding entry in the Materials Project database [64], Miller indices of the particular surface, the bulk lattice type and space group, the magnitude of the moiré reciprocal lattice vector as a percentage of that of graphene $|\epsilon|\%$, the V_1^* value corresponding to the mismatch, the moiré length scale, and the bulk band gap of the substrate.

where $n = 1, 3$ specifies the harmonic and V_n, t_n are real. The model Hamiltonian in Eq. (5) only contains V_1 with no t_n .

The most general crystal-symmetry-allowed form for the second harmonic is

$$H_{G,\pm} = V_2 \pm t_{\perp,2}(\hat{G} \times \tau) \pm it_{z,2}\tau_z, \quad (20)$$

where $V_2, t_{\perp,2}$, and $t_{z,2}$ are real. The $t_{z,2}$ term takes opposite sign for G and $-G$, whereas all other contributions take the same sign for both. None of these terms appear in the original half-chiral model.

In the presence of these additional terms, the Fermi velocity can always be tuned to zero by a single tuning parameter, which may physically correspond to lattice mismatch or pressure [42]. In general, the magic value of V_1 will be changed. Our numerical calculations of the band structure show that the only parameter which significantly changes the magic value is $t_{\perp,2}$ which adds a linear order correction to V_1^* , as shown in Fig. 5a. The other chiral-symmetry-breaking terms add quadratic order corrections.

Moreover, terms which do not break the chiral symmetry (in these lowest few harmonics, $t_{\perp,2}$ and V_3) cannot break the perfect flatness of the bands, according to the symmetry arguments given in Ref. [42]. Terms that break chiral symmetry, however, generally introduce a band dispersion, as shown in Fig. 5b. Representative spectra are shown in Fig. 5c.

2. Crystal symmetry breaking

In realistic implementations, many of the crystal symmetries of graphene will generically be broken by the substrate. In this section, motivated by our material candidates in Table II, we will assume that $SU(2)_{\text{spin}}$, time reversal, and C_{3z} symmetry are preserved.

The remaining crystal symmetries are M_z , the twofold rotations $C_{2x,y,z}$, the in-plane mirror symmetries $M_{x,y}$, and spatial inversion I . The last six can be broken into two classes: those which preserve the z -orientation (M_x, M_y , and C_{2z}), and those which flip it (C_{2y}, C_{2x} , and I). Each term in the second class is the product of an element in the first class and M_z . The latter class of symmetries is necessarily broken when graphene sits on top of the substrate, as shown in Fig. 6a. If instead graphene is sandwiched between two symmetry-related substrate layers, as shown in Fig. 6b, exactly one of these symmetries can be restored.

We now look to the physical symmetries of the substrates in Table II. Analyzing the symmetry groups reveals that all of our material candidates have M_x , the reflection sending $x \mapsto -x$. In principle, it is always possible to restore both M_x and C_{2x} (and therefore $I = C_{2x}M_x$) in a sandwich structure. Therefore, in such a setup, none of the crystal symmetries in the effective model are broken.

However, since the sandwich structure may be difficult to achieve, and, further, makes it challenging to probe the

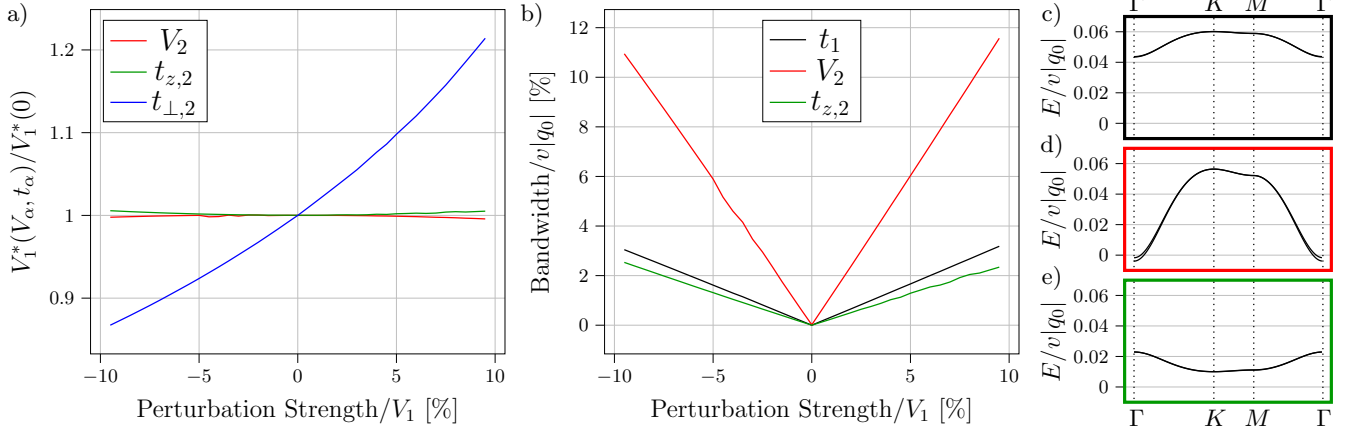


FIG. 5. Corrections to the half-chiral model induced by small symmetry-preserving perturbations of the lowest two harmonics. (a) Only the $t_{\perp,2}$ term (blue) significantly changes the Fermi-velocity-minimizing value of V_1^* . The next-largest corrections come from V_2 (red) and $t_{z,2}$ (green). (b) Bandwidth as a function of t_1 (black), $t_{z,2}$ (green), and V_2 (red). (c-e) Representative spectra for those perturbations which induce bandwidth: (c) t_1 , (d) V_2 , and (e) $t_{z,2}$.

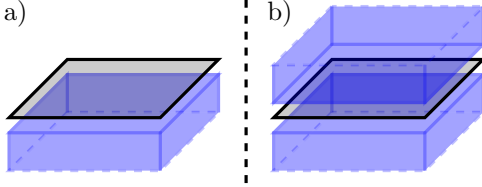


FIG. 6. (a) Graphene on a substrate manifestly breaks the out of plane rotations C_{2x} and C_{2y} . (b) A sandwiched heterostructure can preserve C_{2x} or C_{2y} symmetry.

embedded graphene layer, we restrict ourselves to studying the stacked structure shown in Fig. 6a. Thus, we will consider C_{2y} , C_{2x} and inversion symmetry to be broken. Since those substrates also lack M_y and C_{2z} , we now consider all perturbations compatible with $SU(2)_{\text{spin}}$, C_{3z} , T , and M_x symmetries.

For the first and third harmonics, this extension is remarkably simple: the coefficients $V_{1,3}$ and $t_{1,3}$ are allowed to become complex. For the second harmonic, a new term $H_{G,\pm} = \pm it_{\parallel,2}(\hat{G} \cdot \tau)$ is allowed, where $t_{\parallel,2}$ is real and identical for G and $-G$.

Suppose one considers C_{2z} -breaking in the lowest-harmonic onsite potential, which manifests as a phase on V_1 (with other perturbations vanishing). This arises when the potential in Eq. (3) has a sine as well as a cosine component. The complex phase on V_1 can be eliminated by a basis change $\mathcal{U}_0 = e^{i\theta\mu_z/2}$, where θ is the phase on V_1 , which yields exactly the form in Eq. (4). Thus, the mapping of the near- $\sqrt{3}$ matched potential model to chiral TBG is still valid with a sine component in the potential of Eq. (3).

In fact, our numerical calculations show that *none* of these C_{2x} -breaking perturbations induce a significant

bandwidth or a significant change in the magic value of V_1 . This lack of bandwidth is not implied by the symmetry arguments of Ref. [42].

V. CONCLUSION

In this manuscript, we have comprehensively studied a realization of the half-chiral model by imposing a near- $\sqrt{3}$ matched superlattice potential on a graphene monolayer. The half-chiral model reproduces most of the single-particle and interacting physics of the chiral model for TBG, albeit with half the degrees of freedom. The main difference between the half-chiral model presented here and the chiral model of TBG is in the physical properties of the excitations. For instance, valley-skyrmions are absent in our half-chiral model. Consequently, a realization of the half-chiral model may be a good platform to test which phases of TBG rely on the existence of such skyrmions.

While preliminary data on a SiC/graphene heterostructure has already substantiated the relevance of our model [40], reaching the flat band limit will require a stronger coupling, a closer lattice match, and mitigating symmetry breaking effects. In Table II we propose several other material candidates. An important future question is whether these materials have potential to realize the flat band limit.

Our work will catalyze further design of novel heterostructures realizing analytically or numerically tractable moiré models. Understanding these systems provides insight into the many-body physics of TBG.

VI. ACKNOWLEDGEMENTS

We acknowledge insightful discussions with B. Lian, C. Répellin, and M. Scheer. V.C. is also grateful to N. Regnault for reviewing results from the TBG series [8–13]. J.B., J.C., V.C., and D.G. acknowledge support from the Flatiron Institute, a division of the Simons Foundation. Work by A.D. is supported by the Na-

tional Science Foundation under the Columbia MRSEC on Precision-Assembled Quantum Materials (PAQM), Grant No. DMR-2011738. J.C. acknowledges the Alfred P. Sloan Foundation through a Sloan Research Fellowship and hospitality by the Kavli Institute for Theoretical Physics, where this research was supported in part by the National Science Foundation under Grant No. NSF PHY-1748958.

-
- [1] Y. Cao, V. Fatemi, A. Demir, S. Fang, S. L. Tomarken, J. Y. Luo, J. D. Sanchez-Yamagishi, K. Watanabe, T. Taniguchi, E. Kaxiras, *et al.*, Correlated insulator behaviour at half-filling in magic-angle graphene superlattices, *Nature* **556**, 80 (2018).
 - [2] Y. Cao, V. Fatemi, S. Fang, K. Watanabe, T. Taniguchi, E. Kaxiras, and P. Jarillo-Herrero, Unconventional superconductivity in magic-angle graphene superlattices, *Nature* **556**, 43 (2018).
 - [3] E. Y. Andrei and A. H. MacDonald, Graphene bilayers with a twist, *Nature materials* **19**, 1265 (2020).
 - [4] E. Y. Andrei, D. K. Efetov, P. Jarillo-Herrero, A. H. MacDonald, K. F. Mak, T. Senthil, E. Tutuc, A. Yazdani, and A. F. Young, The marvels of moiré materials, *Nature Reviews Materials* **6**, 201 (2021).
 - [5] G. Tarnopolsky, A. J. Kruchkov, and A. Vishwanath, Origin of magic angles in twisted bilayer graphene, *Physical review letters* **122**, 106405 (2019).
 - [6] J. L. Dos Santos, N. Peres, and A. C. Neto, Graphene bilayer with a twist: electronic structure, *Physical review letters* **99**, 256802 (2007).
 - [7] R. Bistritzer and A. H. MacDonald, Moiré bands in twisted double-layer graphene, *Proceedings of the National Academy of Sciences* **108**, 12233 (2011).
 - [8] B. A. Bernevig, Z.-D. Song, N. Regnault, and B. Lian, Twisted bilayer graphene. i. matrix elements, approximations, perturbation theory, and a $k \cdot p$ two-band model, *Physical Review B* **103**, 205411 (2021).
 - [9] Z.-D. Song, B. Lian, N. Regnault, and B. A. Bernevig, Twisted bilayer graphene. ii. stable symmetry anomaly, *Physical Review B* **103**, 205412 (2021).
 - [10] B. A. Bernevig, Z.-D. Song, N. Regnault, and B. Lian, Twisted bilayer graphene. iii. interacting hamiltonian and exact symmetries, *Physical Review B* **103**, 205413 (2021).
 - [11] B. Lian, Z.-D. Song, N. Regnault, D. K. Efetov, A. Yazdani, and B. A. Bernevig, Twisted bilayer graphene. iv. exact insulator ground states and phase diagram, *Physical Review B* **103**, 205414 (2021).
 - [12] B. A. Bernevig, B. Lian, A. Cowsik, F. Xie, N. Regnault, and Z.-D. Song, Twisted bilayer graphene. v. exact analytic many-body excitations in coulomb hamiltonians: Charge gap, goldstone modes, and absence of cooper pairing, *Physical Review B* **103**, 205415 (2021).
 - [13] F. Xie, A. Cowsik, Z.-D. Song, B. Lian, B. A. Bernevig, and N. Regnault, Twisted bilayer graphene. vi. an exact diagonalization study at nonzero integer filling, *Physical Review B* **103**, 205416 (2021).
 - [14] V. Crépel and L. Fu, Anomalous hall metal and fractional chern insulator in twisted transition metal dichalcogenides, *arXiv preprint arXiv:2207.08895* (2022).
 - [15] Y. Mao, D. Guerci, and C. Mora, Supermoiré low-energy effective theory of twisted trilayer graphene, *Physical Review B* **107**, 125423 (2023).
 - [16] A. Dunbrack and J. Cano, Magic angle conditions for twisted 3d topological insulators, *arXiv preprint arXiv:2112.11464* (2021).
 - [17] V. Crépel, T. Cea, L. Fu, and F. Guinea, Unconventional superconductivity due to interband polarization, *Physical Review B* **105**, 094506 (2022).
 - [18] S. A. A. Ghorashi, A. Dunbrack, A. Abouelkomsan, J. Sun, X. Du, and J. Cano, Topological and stacked flat bands in bilayer graphene with a superlattice potential, *Phys. Rev. Lett.* **130**, 196201 (2023).
 - [19] A. Dunbrack and J. Cano, Intrinsically-multilayer moiré heterostructures, *arXiv preprint arXiv:2301.01777* (2023).
 - [20] V. Crépel, D. Guerci, J. Cano, J. Pixley, and A. Millis, Topological superconductivity in doped magnetic moiré semiconductors, *arXiv preprint arXiv:2304.01631* (2023).
 - [21] V. Crépel, N. Regnault, and R. Queiroz, The chiral limits of moiré semiconductors: origin of flat bands and topology in twisted transition metal dichalcogenides homobilayers, *arXiv e-prints*, *arXiv:2305.10477* (2023), *arXiv:2305.10477 [cond-mat.mes-hall]*.
 - [22] A. L. Sharpe, E. J. Fox, A. W. Barnard, J. Finney, K. Watanabe, T. Taniguchi, M. A. Kastner, and D. Goldhaber-Gordon, Emergent ferromagnetism near three-quarters filling in twisted bilayer graphene, *Science* **365**, 605 (2019).
 - [23] M. Serlin, C. L. Tschirhart, H. Polshyn, Y. Zhang, J. Zhu, K. Watanabe, T. Taniguchi, L. Balents, and A. F. Young, Intrinsic quantized anomalous hall effect in a moiré heterostructure, *Science* **367**, 900 (2020).
 - [24] K. P. Nuckolls, M. Oh, D. Wong, B. Lian, K. Watanabe, T. Taniguchi, B. A. Bernevig, and A. Yazdani, Strongly correlated chern insulators in magic-angle twisted bilayer graphene, *Nature* **588**, 610 (2020).
 - [25] Y. Saito, J. Ge, L. Rademaker, K. Watanabe, T. Taniguchi, D. A. Abanin, and A. F. Young, Hofstadter subband ferromagnetism and symmetry-broken chern insulators in twisted bilayer graphene, *Nature Physics* **17**, 478 (2021).
 - [26] S. Wu, Z. Zhang, K. Watanabe, T. Taniguchi, and E. Y. Andrei, Chern insulators, van hove singularities and topological flat bands in magic-angle twisted bilayer graphene, *Nature Materials* **20**, 488 (2021).
 - [27] M. Garnier, A. Mesaros, and P. Simon, Topological superconductivity with deformable magnetic skyrmions, *Communications Physics* **2**, 126 (2019).

- [28] E. Khalaf, S. Chatterjee, N. Bultinck, M. P. Zaletel, and A. Vishwanath, Charged skyrmions and topological origin of superconductivity in magic-angle graphene, *Science advances* **7**, eabf5299 (2021).
- [29] S. Chatterjee, M. Ippoliti, and M. P. Zaletel, Skyrmion superconductivity: Dmrg evidence for a topological route to superconductivity, *Physical Review B* **106**, 035421 (2022).
- [30] J. Wang, Y. Zheng, A. J. Millis, and J. Cano, Chiral approximation to twisted bilayer graphene: Exact intravalley inversion symmetry, nodal structure, and implications for higher magic angles, *Physical Review Research* **3**, 023155 (2021).
- [31] Y. Sheffer and A. Stern, Chiral magic-angle twisted bilayer graphene in a magnetic field: Landau level correspondence, exact wave functions, and fractional chern insulators, *Physical Review B* **104**, L121405 (2021).
- [32] B. Estienne, N. Regnault, and V. Crépel, Ideal chern bands are landau levels in curved space, *arXiv preprint arXiv:2304.01251* (2023).
- [33] P. J. Ledwith, G. Tarnopolsky, E. Khalaf, and A. Vishwanath, Fractional chern insulator states in twisted bilayer graphene: An analytical approach, *Physical Review Research* **2**, 023237 (2020).
- [34] V. Crépel, B. Estienne, B. A. Bernevig, P. Lecheminant, and N. Regnault, Matrix product state description of halperin states, *Physical Review B* **97**, 165136 (2018).
- [35] J. Wang, J. Cano, A. J. Millis, Z. Liu, and B. Yang, Exact landau level description of geometry and interaction in a flatband, *Physical review letters* **127**, 246403 (2021).
- [36] V. Crépel, N. Regnault, and B. Estienne, Matrix product state description and gaplessness of the haldane-rezayi state, *Physical Review B* **100**, 125128 (2019).
- [37] Y. Xie, A. T. Pierce, J. M. Park, D. E. Parker, E. Khalaf, P. Ledwith, Y. Cao, S. H. Lee, S. Chen, P. R. Forrester, et al., Fractional chern insulators in magic-angle twisted bilayer graphene, *Nature* **600**, 439 (2021).
- [38] N. Bultinck, E. Khalaf, S. Liu, S. Chatterjee, A. Vishwanath, and M. P. Zaletel, Ground state and hidden symmetry of magic-angle graphene at even integer filling, *Physical Review X* **10**, 031034 (2020).
- [39] J. S. Hofmann, E. Khalaf, A. Vishwanath, E. Berg, and J. Y. Lee, Fermionic monte carlo study of a realistic model of twisted bilayer graphene, *Physical Review X* **12**, 011061 (2022).
- [40] Q. Lu, C. Le, X. Zhang, J. Cook, X. He, M. Zarenia, M. Vaninger, P. F. Miceli, D. J. Singh, C. Liu, et al., Dirac fermion cloning, moiré flat bands, and magic lattice constants in epitaxial monolayer graphene, *Advanced Materials* , 2200625 (2022).
- [41] A. Dunbrack and J. Cano, Magic angle conditions for twisted three-dimensional topological insulators, *Phys. Rev. B* **106**, 075142 (2022).
- [42] Y. Sheffer, R. Queiroz, and A. Stern, Symmetries as the guiding principle for flattening bands of dirac fermions (2022).
- [43] M. G. Scheer and B. Lian, Kagome and honeycomb flat bands in moiré graphene (2023), *arXiv:2303.03352 [cond-mat.mes-hall]*.
- [44] A. Dunbrack and J. Cano, Intrinsically-multilayer moiré heterostructures (2023), *arXiv:2301.01777 [cond-mat.mes-hall]*.
- [45] J.-N. Fuchs, Dirac fermions in graphene and analogues: magnetic field and topological properties, *arXiv preprint arXiv:1306.0380* (2013).
- [46] V. Crépel, A. Hackenbroich, N. Regnault, and B. Estienne, Universal signatures of dirac fermions in entanglement and charge fluctuations, *Physical Review B* **103**, 235108 (2021).
- [47] J. Liu, J. Liu, and X. Dai, Pseudo landau level representation of twisted bilayer graphene: Band topology and implications on the correlated insulating phase, *Physical Review B* **99**, 155415 (2019).
- [48] S. Becker, M. Embree, J. Wittsten, and M. Zworski, Mathematics of magic angles in a model of twisted bilayer graphene, *Probability and Mathematical Physics* **3**, 69 (2022).
- [49] S. L. Sondhi, A. Karlhede, S. Kivelson, and E. Rezayi, Skyrmions and the crossover from the integer to fractional quantum hall effect at small zeeman energies, *Physical Review B* **47**, 16419 (1993).
- [50] S. M. Girvin, Spin and isospin: exotic order in quantum hall ferromagnets, *Phys. Today* **53**, 39 (2000).
- [51] Q. Niu, D. J. Thouless, and Y.-S. Wu, Quantized hall conductance as a topological invariant, *Physical Review B* **31**, 3372 (1985).
- [52] H. B. Nielsen and S. Chadha, On how to count goldstone bosons, *Nuclear Physics B* **105**, 445 (1976).
- [53] H. Watanabe and H. Murayama, Unified description of nambu-goldstone bosons without lorentz invariance, *Physical Review Letters* **108**, 251602 (2012).
- [54] C. Forsythe, X. Zhou, K. Watanabe, T. Taniguchi, A. Papsupathy, P. Moon, M. Koshino, P. Kim, and C. R. Dean, Band structure engineering of 2d materials using patterned dielectric superlattices, *Nature nanotechnology* **13**, 566 (2018).
- [55] Y. Li, S. Dietrich, C. Forsythe, T. Taniguchi, K. Watanabe, P. Moon, and C. R. Dean, Anisotropic band flattening in graphene with one-dimensional superlattices, *Nature Nanotechnology* **16**, 525 (2021).
- [56] D. Barcons Ruiz, H. Herzig Sheinflux, R. Hoffmann, I. Torre, H. Agarwal, R. K. Kumar, L. Vistoli, T. Taniguchi, K. Watanabe, A. Bachtold, and F. H. L. Koppens, Engineering high quality graphene superlattices via ion milled ultra-thin etching masks, *Nature Communications* **13**, 1 (2022).
- [57] L.-k. Shi, J. Ma, and J. C. Song, Gate-tunable flat bands in van der waals patterned dielectric superlattices, *2D Materials* **7**, 015028 (2019).
- [58] J. Cano, S. Fang, J. H. Pixley, and J. H. Wilson, Moiré superlattice on the surface of a topological insulator, *Phys. Rev. B* **103**, 155157 (2021).
- [59] T. Wang, N. F. Q. Yuan, and L. Fu, Moiré surface states and enhanced superconductivity in topological insulators, *Phys. Rev. X* **11**, 021024 (2021).
- [60] D. Guerci, J. Wang, J. Pixley, and J. Cano, Designer meron lattice on the surface of a topological insulator, *Physical Review B* **106**, 245417 (2022).
- [61] S. A. A. Ghorashi and J. Cano, Multilayer graphene with a superlattice potential, *arXiv preprint arXiv:2212.12549* (2022).
- [62] H. Ding, S. S. Dwaraknath, L. Garten, P. Ndione, D. Ginley, and K. A. Persson, Computational approach for epitaxial polymorph stabilization through substrate selection, *ACS Applied Materials & Interfaces* **8**, 13086 (2016).
- [63] K. A. Persson, B. Waldwick, P. Lazic, and G. Ceder, Prediction of solid-aqueous equilibria: Scheme to combine

first-principles calculations of solids with experimental aqueous states, Phys. Rev. B **85**, 235438 (2012).

- [64] A. Jain, S. P. Ong, G. Hautier, W. Chen, W. D. Richards, S. Dacek, S. Cholia, D. Gunter, D. Skinner, G. Ceder, and K. A. Persson, Commentary: The materials project: A materials genome approach to accelerating materials innovation, APL Materials **1**, 011002 (2013).
- [65] S. P. Ong, S. Cholia, A. Jain, M. Brafman, D. Gunter, G. Ceder, and K. A. Persson, The materials application programming interface (api): A simple, flexible and efficient api for materials data based on representational state transfer (rest) principles, Computational Materials Science **97**, 209 (2015).
- [66] A. Zur and T. C. McGill, Lattice match: An application to heteroepitaxy, Journal of Applied Physics **55**, 378 (1984).

Appendix A: Projection of onsite potential

In this appendix, we derive the projected Hamiltonian in Eq. (4) from Eqs. (1) and (3). For convenience, we rewrite the potential in Eq. (3) here as

$$V(r) = V_1 \sum_n [e^{iK_n \cdot r} e^{i\epsilon K_n \cdot r} + c.c.]. \quad (\text{A1})$$

We define the Bloch basis:

$$\psi_{k,A/B}(r) = \frac{1}{\sqrt{N}} \sum_R \varphi(r - R_{A/B}) e^{ik \cdot R_{A/B}} \quad (\text{A2})$$

where $R_{A/B} = R \pm u$, R is the lattice vector of graphene, N the number of unit cells, $u = (r_A - r_B)/2 = a(1,0)$ and $\varphi(r - R_{A/B})$ is the p_z orbital of the carbon atoms. Projecting the potential on the Bloch basis we find

$$V_{\alpha,\beta}(k, k') = \frac{\delta_{\alpha\beta}}{N} \sum_R V(R + u_\alpha) e^{-i(k-k')(R+u_\alpha)}, \quad (\text{A3})$$

where $\alpha = A, B$, $u_{A/B} = \pm u$ and we have employed the relation

$$\int d^2\mathbf{r} \varphi^*(r - R_\alpha) V(r) \varphi(r - R_\beta) = \delta_{\alpha\beta} V(R_\alpha). \quad (\text{A4})$$

We first observe that the wave vectors K_n in $V(r)$ connects the two Dirac cones of graphene, $K - K' = K_n + G_n$ with $G = [0, -e_-, -e_+]$ for $n = 0, 1, 2$. The long wavelength modulation $q_n = \epsilon K_n$ gives rise to the moiré lattice in Fig. 1 and introduces the momentum selection rule $\bar{k} - \bar{k}' = q_n$ where \bar{k} and \bar{k}' are small variations around K and K' . As a result, in the sublattice basis $[A, B]$ the matrix element A3 takes the form

$$V_{K,K'}(\bar{k}, \bar{k}') = V_1 \sum_{n=0}^2 \delta_{\bar{k}-\bar{k}', q_n} \begin{bmatrix} e^{-iu \cdot G_n} & 0 \\ 0 & e^{iu \cdot G_n} \end{bmatrix}, \quad (\text{A5})$$

where we defined $V_{K\alpha, K'\beta}(\bar{k}, \bar{k}') \equiv V_{\alpha,\beta}(K + \bar{k}, K' + \bar{k}')$. Noticing that $e_+ = K_0 - K_1$ and $g_- = K_0 - K_2$ we find $e_+ \cdot u = -K_1 \cdot u = -\phi = 2\phi$ and $e_- \cdot u = -K_2 \cdot u = \phi$

where we used the relation $K_n \cdot (r_A - r_B) = 2K_n \cdot u = 2n\phi$. Finally, we find

$$V_{K,K'}(\bar{k}, \bar{k}') = V_1 \sum_n \delta_{\bar{k}, \bar{k}'+q_n} \begin{bmatrix} e^{in\phi} & 0 \\ 0 & e^{-in\phi} \end{bmatrix}, \quad (\text{A6})$$

which in real space becomes Eq. (4).

Appendix B: Charge gap

In this appendix, we study the charged excitations above the ferromagnetic ground state at filling $n = -1$. We choose the ground state to be polarized in the $\alpha = (-, \downarrow)$ flavor, $|\text{FM}\rangle = \prod_k c_{k,-,\downarrow}^\dagger |\emptyset\rangle$, with $|\emptyset\rangle$ the state with all bands empty (filling $n = -2$). The charged excitations are accompanied by either a spin flip, a chirality flip, or both:

$$\begin{aligned} |\phi_S(k)\rangle &= c_{k,-,\uparrow}^\dagger |\text{FM}\rangle, \\ |\phi_\Lambda(k)\rangle &= c_{k,+, \downarrow}^\dagger |\text{FM}\rangle, \\ |\phi_T(k)\rangle &= c_{k,+, \uparrow}^\dagger |\text{FM}\rangle. \end{aligned} \quad (\text{B1})$$

Since the Hamiltonian is translation invariant, the momentum k of these states is conserved and finding the dispersion of these charged excitations only involves diagonalizing a 3×3 matrix.

Away from $\alpha = \alpha^*$, the band and chirality indices are no longer identical and the band eigenmodes $d_{k,n=\pm,\sigma}$ with energy $n\varepsilon_k$, can be expressed as linear combinations of the chiral fermionic operators $c_{k,\gamma=\pm,\sigma}$. Since Λ_z anticommutes with the Hamiltonian, the dispersion must be off-diagonal when written in the chiral basis

$$H_k = \sum_{k,n,\sigma} n\varepsilon_k d_{n,\sigma}^\dagger d_{n,\sigma} = \sum_{k,\sigma} [u_k c_{k,+, \sigma}^\dagger c_{k, -, \sigma} + hc], \quad (\text{B2})$$

where the u_k are determined numerically by projection. Finally, recall that the interaction

$$H_{\text{int}} = \frac{1}{2} U_{(\alpha,\beta)}(k_1, k_2, q) c_{k_1, \alpha}^\dagger c_{k_1+q, \alpha} c_{k_2+q, \beta}^\dagger c_{k_2, \beta}, \quad (\text{B3})$$

has diagonal form factors in the chiral basis

$$U_{(\alpha,\beta)}(k_1, k_2, q) = \sum_G U_{q+G} F_{k_1, q+G}^\alpha F_{k_2, q+G}^{\beta*}. \quad (\text{B4})$$

Finding the dispersion of a charged excitation above the ferromagnet $|\text{FM}\rangle$ amounts to diagonalizing the kinetic and interacting Hamiltonian in the $[\phi_\Lambda(k), \phi_T(k), \phi_S(k)]$ subspace, where the matrix elements read

$$H_k = \begin{bmatrix} I_{\text{FM}}(k) & 0 & 0 \\ 0 & I_{\text{FM}}^*(k) & u_k \\ 0 & u_k^* & I_{\text{FM}}(k) \end{bmatrix} \quad (\text{B5})$$

and Wick contractions provide the simple form

$$I_M(k) = \sum_q U_{M, \text{FM}}(k, q, 0) + U_{M, M}(k, k, q)/2. \quad (\text{B6})$$

Finally, since our flavor-flip analysis serves the purpose of illustrating the effects of interactions in our model, we model the electronic repulsion with a positive term $U_q = U > 0$ for all q , *i.e.* a local repulsion between all flavors in real-space. In Fig. 4, we have used an interaction amplitude $U = 0.5|vq_0|$.

Appendix C: Charge neutral excitations

1. Setup

The neutral excitations above the Chern insulating ground state at $n = \pm 1$ are of three different types: spin-flipping (S), chirality-flipping (Λ) and spin-chirality-flipping (T). They respectively take the form

$$\begin{aligned} |k, S\rangle_Q &= c_{k+Q, -, \uparrow}^\dagger c_{k, -, \downarrow} |\text{FM}\rangle, \\ |k, \Lambda\rangle_Q &= c_{k+Q, +, \downarrow}^\dagger c_{k, -, \downarrow} |\text{FM}\rangle, \\ |k, T\rangle_Q &= c_{k+Q, +, \uparrow}^\dagger c_{k, -, \downarrow} |\text{FM}\rangle. \end{aligned} \quad (\text{C1})$$

Since the Hamiltonian is translation invariant, the center of mass momentum Q is conserved, and we shall leave it implicit when no confusion is possible.

The well-defined spin S_z and Λ_z quantum number of the excitations in Eq. (C1) only allow for a few non-zero elements of the kinetic Hamiltonian defined in Eq. (B2), which are given by

$$\langle k', S | H_k | k, T \rangle = \langle k, T | H_k | k', S \rangle^* = \delta_{k', k} u_{k+Q}. \quad (\text{C2})$$

The matrix elements of H_1 in the basis of single particle excitations Eq. (C1) can be obtained using Wick contractions. In the chiral limit, where the form factor is diagonal in the chiral basis, as shown in Sec. III A, they only couple states with the same flavor-flip $\langle k', M | H_1 | k, N \rangle = \delta_{M, N} \langle k' | H_1 | k \rangle_M$, and take the following form

$$\begin{aligned} \langle k' | H_1 | k \rangle_M &= -U_{M, \text{FM}}(k + Q, k, k' - k) \\ &+ \delta_{k', k} \sum_{\tilde{k}} [U_{M, \text{FM}}(k + Q, \tilde{k}, 0) - U_{\text{FM}, \text{FM}}(k, \tilde{k}, 0)] \\ &+ \delta_{k', k} \sum_{\tilde{k}} [U_{\text{FM}, \text{FM}}(k, k, \tilde{k}) + U_{M, M}(k + Q, k + Q, \tilde{k})]/2, \end{aligned} \quad (\text{C3})$$

which was decomposed into a direct electron-hole interaction (first line), an electron and hole Hartree contribution (second line), and a sum of Fock terms (third line). In this calculation, we have subtracted the interaction energy of the $|\text{FM}\rangle$ state, as in Appendix B, and used the relation $U_{\beta\alpha}(k_2 + q, k_1 + q, -q) = U_{\alpha\beta}(k_1, k_2, q)$ which only holds true for inversion symmetric Coulomb potentials $U_{-q} = U_q$.

Once these coefficients have been computed, collective excitations above $|\text{FM}\rangle$ are obtained by diagonalizing

$$\langle k' | H_1 | k \rangle_{\overline{\text{FM}}}, \quad \begin{bmatrix} \langle k' | H_1 | k \rangle_{\overline{\text{FM}}} & \text{diag}(u_{k+Q}) \\ \text{diag}(u_{k+Q}^*) & \langle k' | H_1 | k \rangle_{\text{FM}} \end{bmatrix}, \quad (\text{C4})$$

corresponding to the Λ and (S, T) subspaces. Note that each block represented by its (k', k) elements is a matrix whose dimension equals the number of Brillouin zone points.

2. Chiral limit

To start with we consider the magic angle case $\alpha = \alpha^*$, for which $u_k = 0$, and where Fig. 4c shows a gapless quadratic branch and a few gapped modes below the many-body continuum. We can capture these features using a small Q Taylor expansion.

Let us first show that the lowest energy mode of the spin-flipping S branch has exactly zero energy at $Q = 0$ by diagonalizing the interaction term in the $M = \text{FM}$ sector. Clearly, the Hartree contribution at $Q = 0$ vanishes in this sector (see Eq. (C3)). While the diagonal Fock term is positive, it is precisely opposite to the sum of the direct interaction matrix elements along each row $\sum_{k'} \langle k' | H_1 | k \rangle_{\text{FM}} = 0$. By the Gershgorin circle theorem, this ensures that all eigenvalues of the interaction in the FM sector are non-negative. The lowest possible value, zero, is reached by a vector \mathbf{V}_{mag} whose coefficients are all equal corresponding to the Goldstone mode associated with the breaking of the $\text{SU}(2)_{\text{Spin}}$ symmetry. In the $\overline{\text{FM}}$ sector at $Q = 0$ we have the additional positive Hartree term $\delta_{k', k} \sum_{\tilde{k}} [U_{\overline{\text{FM}}, \text{FM}}(k, \tilde{k}, 0) - U_{\text{FM}, \text{FM}}(k, \tilde{k}, 0)]$, see second line of Eq. (C3). The latter introduces a gap $\Delta_n > 0$ for the first few chiral-breaking excitations $\mathbf{V}_{Z2}^{(n)}$ with $n = 1, 2, 3 \dots$ (in the T and Λ sectors); the subscript Z2 refers to the chiral-flip character of these collective modes.

The Goldstone mode dispersion around γ is quadratic in Q as expected from general arguments [53]. To prove the vanishing of the linear term we perform a $k \cdot p$ expansion around γ ,

$$\begin{aligned} \epsilon_Q^{\text{mag}} &\simeq Q \cdot [\mathbf{V}_{\text{mag}}^\dagger (\nabla_Q H_1) \mathbf{V}_{\text{mag}}] \\ &= Q \cdot \nabla_Q \left[\frac{1}{N_{BZ}} \sum_{k, k'} \langle k' | H_1 | k \rangle_{\text{FM}} \right], \end{aligned} \quad (\text{C5})$$

with N_{BZ} the number of point in the Brillouin zone. We now look at coefficient of the linear in momentum term:

$$\begin{aligned} \frac{\nabla Q}{N_{BZ}} \sum_{k,k'} \langle k' | H_I | k \rangle_{\text{FM}} &= \sum_{k,q} \sum_G \frac{U_{q+G}}{N_{BZ}^2} \text{Re} \left[F_{k,q+G}^{-*} \left(\nabla_k F_{k,q+G}^- \right) \right] + \sum_G \frac{U_G}{N_{BZ}^2} \left[\sum_p \nabla_p F_{p,G}^- \right] \left[\sum_k F_{k,G}^{-*} \right] \\ &- \sum_{k,k'} \sum_G \frac{U_{k-k'+G}}{N_{BZ}^2} F_{k',k-k'+G}^{-*} \left[\langle \psi_{k',-} | \nabla_k \psi_{k+G,-} \rangle + \langle \nabla_{k'} \psi_{k',-} | \psi_{k+G,-} \rangle \right]. \end{aligned} \quad (\text{C6})$$

Making the change of variables $q = k' - k$ yields

$$\begin{aligned} \frac{\nabla Q}{N_{BZ}} \sum_{k,k'} \langle k' | H_I | k \rangle_{\text{FM}} &= \sum_{k,q} \sum_G \frac{U_{q+G}}{N_{BZ}^2} \text{Re} \left[F_{k,q+G}^{-*} \left(\nabla_k F_{k,q+G}^- \right) \right] - \sum_{k,q} \sum_G \frac{U_{q+G}}{N_{BZ}^2} F_{k,q+G}^{-*} \left(\nabla_k F_{k,q+G}^- \right) \\ &+ \sum_G \frac{U_G}{N_{BZ}^2} \left[\sum_p \nabla_p F_{p,G}^- \right] \left[\sum_k F_{k,G}^{-*} \right]. \end{aligned} \quad (\text{C7})$$

By sending $q \rightarrow -q$, $G \rightarrow -G$, using the relation $U_q = U_{-q}$ we readily find that the second contribution on the right hand side of Eq. (C7) is real and cancels the first one. We are left with

$$\frac{\nabla Q}{N_{BZ}} \sum_{k,k'} \langle k' | H_I | k \rangle_{\text{FM}} = \sum_{p,k,G} \frac{U_G}{N_{BZ}^2} (\nabla_p F_{p,G}^-) F_{k,G}^{-*}. \quad (\text{C8})$$

To show the vanishing of the right hand side we first make the change of variable $p' = C_{3z} p$ so that $(\nabla_p F_{p,G}^-) = (C_{3z} \nabla_{p'} F_{C_{3z}^{-1} p', G}^-)$. Then, we use the C_{3z} symmetry $F_{C_{3z} p, G}^- = F_{p, C_{3z}^{-1} G}^-$ and $U_{C_{3z} G} = U_G$. Finally, we find:

$$\frac{\nabla Q}{N_{BZ}} \sum_{k,k'} \langle k' | H_I | k \rangle_{\text{FM}} = C_{3z} \sum_{p,k,G} \frac{U_G}{N_{BZ}^2} (\nabla_p F_{p,G}^-) F_{k,G}^{-*}, \quad (\text{C9})$$

i.e. $C_{3z} v = v$ with v two-dimensional vector, which implies

$$\frac{\nabla K}{N_{BZ}} \sum_{k,k'} \langle k' | H_I | k \rangle_{\text{FM}} = 0. \quad (\text{C10})$$

The dispersion of the Goldstone modes goes like Q^2 for small Q , i.e.,

$$\epsilon_Q^{\text{mag}} = \frac{1}{2} m_{ij} Q_i Q_j \quad (\text{C11})$$

where

$$\begin{aligned} m_{ij} &= \mathbf{V}_{\text{mag}}^\dagger (\partial_i \partial_j H_I) \mathbf{V}_{\text{mag}} \\ &- 2 \sum_{n \neq \text{mag}} \frac{(\mathbf{V}_{\text{mag}}^\dagger \partial_i H_I \mathbf{V}_{Z2}^{(n)}) (\mathbf{V}_{Z2}^{(n)} \partial_j H_I \mathbf{V}_{\text{mag}})}{\Delta_n}, \end{aligned} \quad (\text{C12})$$

with $\partial_i = \partial_{Q_i}$ derivative with respect to the center of mass momentum Q and Δ_n is the energy of the chiral-flip mode $\mathbf{V}_{Z2}^{(n)}$.

3. Reference kinetic energy

In this section we highlight the effect of finite dispersion away from the magic angle condition in the chiral

limit. We now derive the kinetic energy gain of the ferromagnetic ground state. To find it, we note that the $|\text{FM}\rangle$ ground state is connected to states in the Λ sector at $Q = 0$ through

$$\begin{bmatrix} \langle k' | H_I | k \rangle_{\overline{\text{FM}}} & u_k \\ u_{k'}^T & 0 \end{bmatrix}. \quad (\text{C13})$$

It is important to notice that the latter Hamiltonian coincides precisely the matrix that couples \mathbf{V}_{mag} to the gapped excitation in the $\overline{\text{FM}}$ sector. To second order in perturbation theory, we thus have

$$E_{\text{FM}}^{\text{kin}} \simeq - \sum_n \frac{|\langle \mathbf{V}_{Z2}^{(n)} | u_k | \mathbf{V}_{\text{mag}} \rangle|}{\Delta_n}, \quad (\text{C14})$$

with Δ_n the energy of $\mathbf{V}_{Z2}^{(n)}$, both for the ferromagnetic state and the $Q = 0$ magnon state. In other words the hybridization induced by the finite bandwidth with the spin-chirality-flipping (T) modes gives rise to the same energy gain in the ferromagnetic ground state and in the $Q = 0$ magnon state. This coincidence of energy level extends to all order in perturbation theory due to the $\text{SU}(2)$ symmetry of the original model [11].

Another way to understand the degeneracy is to momentarily forget to subtract off the ferromagnetic ground state energy. In that case, the energy reduction in Eq. (C14) pulls the $Q = 0$ magnon state below zero energy, hinting that it is the new ferromagnetic ground state of the system. However, \mathbf{V}_{mag} can be regarded as a spin-flip acting on all particles at the same time, or a global spin rotation of $|\text{FM}\rangle$ itself. This would mean that a spin-rotation of the ferromagnet is more stable than the ferromagnet itself, in contradiction with the global $\text{SU}(2)$ symmetry of the problem and its spontaneous symmetry breaking.

Appendix D: Symmetry Analysis

In this appendix, we derive the most general form of the low-energy Hamiltonian that respects time-reversal,

| Hamiltonian Form | | | | | Symmetries | | | |
|------------------|--------|--|----|------|-------------|----------|----------|----------|
| Block | Coeff. | Term | SV | $-G$ | Λ_z | C_{2x} | C_{2y} | C_{2z} |
| H_{\pm} | A | τ_0 | + | | X | ✓ | ✓ | ✓ |
| | B | τ_z | - | | X | ✓ | X | X |
| | C | $k \cdot \tau$ | + | | ✓ | ✓ | ✓ | ✓ |
| | D | $k \times \tau$ | + | | ✓ | X | X | ✓ |
| H_Q | Re B | τ_z | | | X | $-x$ | $+x$ | X |
| | Im B | $i\tau_z$ | | | X | $+x$ | $+x$ | ✓ |
| | Re C | $\hat{Q} \cdot \tau$ | | | ✓ | $-x$ | $-x$ | ✓ |
| | Im C | $i\hat{Q} \cdot \tau$ | | | ✓ | $+x$ | $-x$ | X |
| | Re D | $(\hat{Q} \times \tau) \cdot \hat{z}$ | | | ✓ | $+x$ | $+x$ | ✓ |
| | Im D | $i(\hat{Q} \times \tau) \cdot \hat{z}$ | | | ✓ | $-x$ | $+x$ | X |
| $H_{G,\pm}$ | Re A | τ_0 | + | + | X | $+x, +y$ | $+x, +y$ | ✓ |
| | Im A | $i\tau_0$ | + | - | X | $-x, +y$ | $+x, -y$ | X |
| | Re B | τ_z | - | + | X | $+x, +y$ | $-x, -y$ | X |
| | Im B | $i\tau_z$ | - | - | X | $-x, +y$ | $-x, +y$ | ✓ |
| | Re C | $\hat{G} \cdot \tau$ | - | - | ✓ | $+x, -y$ | $+x, -y$ | ✓ |
| | Im C | $i\hat{G} \cdot \tau$ | - | + | ✓ | $-x, -y$ | $+x, +y$ | X |
| | Re D | $(\hat{G} \times \tau) \cdot \hat{z}$ | - | - | ✓ | $-x, +y$ | $-x, +y$ | ✓ |
| | Im D | $i(\hat{G} \times \tau) \cdot \hat{z}$ | - | + | ✓ | $+x, +y$ | $-x, -y$ | X |

TABLE III. Terms that can be added with arbitrary real coefficients to the model Hamiltonian in Eq. (5) in the TBG_K basis while respecting time reversal, C_{3z} , and $SU(2)_{\text{Spin}}$ symmetries. The first five columns describe the additional term, as follows: The first column lists to which block of Eq. (D1) the term is added. The second column lists its coefficient in the notation of Eq. (D2), and the third column lists the term itself, for a C_{3z} -related set of Qs/Gs. The fourth column describes the relative sign between the two sublattice-valley combinations (the \pm subscript in H_{\pm} and $H_{G,\pm}$), determined by time-reversal symmetry. The fifth column describes the relative sign between G and $-G$ imposed by hermiticity. The last four columns indicate whether the term respects (✓) or breaks (X) important symmetries of the model. For the C_{2x} and C_{2y} columns, $\pm_{x,y}$ indicates the relative sign of the coefficient when Q, G undergo the reflections $M_{x,y}$.

C_{3z} , and $SU(2)_{\text{Spin}}$ symmetry. The resulting symmetry-allowed terms are summarized in Table III.

We work in the TBG_K basis because the form of C_{3z} symmetry, $\exp(i\pi\tau_z/3)$, is valley-independent, which leads to more elegant expressions. We will also neglect spin entirely due to the assumed $SU(2)$ symmetry.

By arguments analogous to those given in Appendix A, the low-energy effective Hamiltonian takes the form

$$H_{\text{eff}}^{\text{TBG}_K} = \left[\begin{array}{cc} \sum_G H_{G,+} e^{iG \cdot r} & \sum_Q H_Q e^{iQ \cdot r} \\ \sum_Q H_Q^\dagger e^{-iQ \cdot r} & \sum_G H_{G,-} e^{iG \cdot r} \end{array} \right]. \quad (\text{D1})$$

G runs over the moiré reciprocal lattice vectors ϵg (where g is a reciprocal lattice vector of graphene) and Q runs over $G + \epsilon K_0$. In this way, at $\epsilon = 0$, the sum over G describes all harmonics which couple K to itself, and the sum over Q describes all harmonics that couple K to K' .

We compute $H_{G=0,\pm}$ (abbreviated as H_{\pm}) to first order in k , and all other terms to zeroth order in k . The symmetry $C_{3z} = \exp(i\pi\tau_z/3)$ constrains each 2×2 block of the Hamiltonian. The term $H_{G=0,\pm}$ can be written as

$$H_{\pm}(k) = A\tau_0 + B\tau_z + C(k \cdot \tau) + D(k \times \tau) \cdot \hat{z}. \quad (\text{D2})$$

Other harmonics $H_{G,\pm}$ can be expanded with the same coefficients by making the replacement $k \rightarrow \hat{G}$, and similarly H_Q with $k \rightarrow \hat{Q}$.

In this decomposition, the coefficients A - D are the same for C_{3z} -related Qs and Gs. The coefficients are generally complex, but hermiticity imposes the constraint $H_{G,\pm} = H_{-G,\pm}^\dagger$. Therefore, we can derive $A(G) = A(-G)^*$ and $B(G) = B(-G)^*$. Similarly, for $G \neq 0$, we find $C(G) = -C(-G)^*$ and $D(G) = -D(-G)^*$. For the special case $G = 0$, hermiticity implies the coefficients A - D of H_{\pm} are real.

We now derive the constraints from time-reversal symmetry, chiral symmetry, and the remaining crystal symmetries on each of these terms individually; the form of each symmetry operator is listed in Table I. Among these, the terms which respect time reversal are listed in Table III, along with which of the other symmetries they respect.

Note that when considering the action of M_x and M_y constrained to vectors in the plane (such as k, Q , and G), we have $M_x = -M_y$, since $M_x M_y = C_{2z} = -I$.

1. Zeroth harmonic: H_{\pm}

We now consider how symmetry constrains the action of the zeroth harmonic H_{\pm} in terms of the (real) coefficients A - D . Note the \pm sign refers to the sublattice-valley (SV) index, as we are working in the TBG basis; accordingly, we will call the coefficients SV-even (resp. SV-odd) if they take opposite sign (resp. same sign) in the two valleys.

Time reversal relates the two valleys,

$$H_{\pm}(k) = \tau_y H_{\mp}^*(-k) \tau_y, \quad (\text{D3})$$

implying that B must be SV-odd but the other coefficients must be SV-even. The anticommuting chiral symmetry requires

$$H_{\pm}(k) = -\tau_z H_{\pm}(k) \tau_z, \quad (\text{D4})$$

implying $A = B = 0$. $C_{2x}T$ requires

$$H_{\pm}(k) = \tau_z H_{\pm}(M_x k)^* \tau_z, \quad (\text{D5})$$

implying $D = 0$. C_{2y} requires

$$H_{\pm}(k) = \tau_y H_{\pm}(M_y k) \tau_y, \quad (\text{D6})$$

implying $B = D = 0$. Finally, $C_{2z}T$ requires

$$H_{\pm}(k) = \tau_x H_{\pm}(k)^* \tau_x, \quad (\text{D7})$$

implying $B = 0$.

Altogether, the crystal symmetries restrict the form of the zeroth harmonic to $H_{\pm} = A + C(k \cdot \tau)$, which is used in Eq. (18) of the main text.

2. *K-to-K'* harmonics: H_Q

For the off-diagonal terms in Eq. (D1), H_Q , time-reversal implies

$$H_Q = -\tau_y H_Q^T \tau_y, \quad (\text{D8})$$

which implies $A = 0$. The anticommuting chiral symmetry requires

$$H_Q = -\tau_z H_Q \tau_z, \quad (\text{D9})$$

implying $B = 0$. $C_{2z}T$ requires

$$H_Q = \tau_x H_Q^* \tau_x, \quad (\text{D10})$$

implying B is imaginary whereas C and D are real.

In generality, $C_{2x}T$ requires

$$H_Q = -\tau_z H_{M_y Q}^* \tau_z, \quad (\text{D11})$$

whereas C_{2y} requires

$$H_Q = -\tau_y H_{M_x Q} \tau_y. \quad (\text{D12})$$

However, the specific constraints of this action on the coefficients A - D depend on the particular \hat{Q} involved. When the set of C_{3z} -related Q s are closed under $M_x = -M_y$, these properties more stringently constrain the coefficients A - D . This is for instance the case for the first and third harmonics, where one of the Q is in the $\pm\hat{y}$ direction, so the C_{3z} -related set of Q s are closed under $M_x = -M_y$. In these harmonics, C_{2x} implies that B and C are imaginary, whereas D is real; while C_{2y} implies that $C = 0$.

However, not all harmonics have a Q in the $\pm\hat{y}$ direction; for these higher harmonics, C_{2x} and C_{2y} impose the constraint that the coefficients of a C_{3z} -related set of Q s is related to its corresponding mirror.

3. Nonzero *K-to-K* harmonics: $H_{G,\pm}$

Time-reversal symmetry implies

$$H_{G,\pm} = \tau_y H_{-G,\mp}^* \tau_y, \quad (\text{D13})$$

which together with hermiticity, $H_{-G} = H_G^\dagger$, imposes the constraint

$$H_{G,\pm} = \tau_y H_{G,\mp}^T \tau_y. \quad (\text{D14})$$

Therefore, A is SV-even, whereas all other coefficients are SV-odd. Chiral symmetry requires

$$H_{G,\pm} = -\tau_z H_{G,\pm} \tau_z, \quad (\text{D15})$$

implying $A = B = 0$. $C_{2z}T$ requires

$$H_{G,\pm} = \tau_x H_{G,\pm}^* \tau_x, \quad (\text{D16})$$

implying that A , C , and D are real, whereas B is imaginary.

Like H_Q , for $H_{G,\pm}$, specific constraints of C_{2x} and C_{2y} on the coefficients A - D depend on the specific G . In generality, $C_{2x}T$ requires

$$H_{G,\pm} = \tau_z H_{M_y G,\pm}^T \tau_z, \quad (\text{D17})$$

whereas C_{2y} requires

$$H_{G,\pm} = \tau_y H_{M_x G,\pm} \tau_y. \quad (\text{D18})$$

There are three possibilities for the symmetry of a $C_{3z}+T$ -related set of G s under reflections R_x and R_y . They may not be closed under these operations, in which case coefficients at G and $M_x G$ are related. If the set of G for some harmonic are closed under M_x and M_y , then there will be some G in the set which is left fixed under either M_x or M_y ; the constraints on the coefficients depend on which reflection leaves a G fixed.

For the second harmonic, one G lies along the \hat{x} direction, so M_y preserves that G . For this case, C_{2x} implies that $C = 0$, whereas C_{2y} implies that A and C are real while B and D are imaginary.

For the alternative possible higher harmonic, where M_x leaves a G fixed, we find different constraints. C_{2x} implies that A , B , and C are real, whereas D is imaginary. C_{2y} implies that $B = D = 0$.

Appendix E: Additional candidate substrates

See Tables IV and V.

| Composition | mp-id | Surface | Lattice | SG | $ \epsilon /\%$ | V_1^* (meV) | Moiré length (nm) | Gap (eV) |
|------------------------------------|---------|---------|---------|---------------------------|-----------------|---------------|-------------------|----------|
| NaNdSe ₂ | 999471 | 111 | rhomb. | <i>R3m</i> | 0.13 | 9 | 1905 | 1.83 |
| RbH | 24721 | 111 | cubic | <i>Fm3m</i> | 0.14 | 9 | 1777 | 3.20 |
| CsPrS ₂ | 9037 | 001 | hex. | <i>P6₃/mmc</i> | 0.19 | 13 | 1272 | 2.28 |
| RbTbSe ₂ | 10782 | 111 | rhomb. | <i>R3m</i> | 0.27 | 18 | 907 | 2.01 |
| SmTlSe ₂ | 999137 | 111 | rhomb. | <i>R3m</i> | 0.28 | 18 | 897 | 1.42 |
| NaBr | 22916 | 111 | cubic | <i>Fm3m</i> | 0.29 | 19 | 841 | 4.09 |
| SrS | 1087 | 111 | cubic | <i>Fm3m</i> | 0.30 | 20 | 828 | 2.56 |
| RbPrS ₂ | 9362 | 111 | rhomb. | <i>R3m</i> | 0.32 | 21 | 774 | 2.36 |
| Li ₂ Se | 2286 | 111 | cubic | <i>Fm3m</i> | 0.42 | 28 | 586 | 3.11 |
| Sr(Li ₂ P) ₂ | 570097 | 111 | rhomb. | <i>R3m</i> | 0.47 | 31 | 522 | 1.17 |
| CsNdS ₂ | 1095172 | 001 | hex. | <i>P6₃/mmc</i> | 0.55 | 36 | 450 | 2.27 |
| KLaS ₂ | 15781 | 111 | rhomb. | <i>R3m</i> | 0.57 | 37 | 434 | 2.77 |
| BiTeCl | 28944 | 001 | hex. | <i>P6₃mc</i> | 0.66 | 43 | 375 | 1.56 |
| U(OF) ₂ | 27980 | 111 | rhomb. | <i>R3m</i> | 0.67 | 44 | 367 | 2.12 |
| MgSe | 13031 | 111 | cubic | <i>F43m</i> | 0.73 | 48 | 336 | 2.55 |
| GeI ₂ | 27922 | 001 | hex. | <i>P3m1</i> | 0.76 | 50 | 325 | 2.07 |
| KSmSe ₂ | 1006891 | 111 | rhomb. | <i>R3m</i> | 0.77 | 51 | 320 | 1.97 |
| PbF ₂ | 315 | 111 | cubic | <i>Fm3m</i> | 0.79 | 52 | 314 | 4.44 |
| NaPrSe ₂ | 999461 | 111 | rhomb. | <i>R3m</i> | 0.80 | 53 | 307 | 1.83 |
| Ca ₂ PI | 23040 | 111 | rhomb. | <i>R3m</i> | 0.83 | 55 | 297 | 1.80 |
| LaSeF | 7738 | 001 | hex. | <i>P6₃/mmc</i> | 0.90 | 59 | 275 | 1.72 |
| KPrS ₂ | 15782 | 111 | rhomb. | <i>R3m</i> | 0.95 | 62 | 259 | 2.36 |
| RbHoSe ₂ | 10783 | 111 | rhomb. | <i>R3m</i> | 1.07 | 70 | 231 | 2.04 |
| RbNdS ₂ | 9363 | 111 | rhomb. | <i>R3m</i> | 1.07 | 71 | 230 | 2.35 |
| CsF | 1784 | 111 | cubic | <i>Fm3m</i> | 1.19 | 78 | 207 | 5.28 |
| RbLaS ₂ | 9361 | 111 | rhomb. | <i>R3m</i> | 1.20 | 79 | 206 | 2.75 |
| Ba ₂ CuClO ₂ | 551456 | 111 | rhomb. | <i>R3m</i> | 1.29 | 85 | 191 | 2.31 |
| RbSmSe ₂ | 10780 | 111 | rhomb. | <i>R3m</i> | 1.30 | 86 | 189 | 1.98 |
| CaSe | 1415 | 111 | cubic | <i>Fm3m</i> | 1.31 | 86 | 188 | 2.14 |
| NdTlSe ₂ | 568588 | 111 | rhomb. | <i>R3m</i> | 1.31 | 86 | 188 | 1.44 |
| RbErSe ₂ | 10784 | 111 | rhomb. | <i>R3m</i> | 1.41 | 93 | 175 | 2.06 |
| KNdS ₂ | 1006885 | 111 | rhomb. | <i>R3m</i> | 1.44 | 95 | 171 | 2.32 |
| MgI ₂ | 23205 | 001 | hex. | <i>P3m1</i> | 1.49 | 98 | 165 | 3.68 |
| RbNdSe ₂ | 10779 | 111 | rhomb. | <i>R3m</i> | 2.52 | 165 | 98 | 1.97 |
| SrLiP | 13276 | 001 | hex. | <i>P6₃/mmc</i> | 2.54 | 167 | 97 | 1.35 |
| NaLaSe ₂ | 999472 | 111 | rhomb. | <i>R3m</i> | 2.55 | 168 | 97 | 2.35 |
| CsGdS ₂ | 9084 | 111 | rhomb. | <i>R3m</i> | 2.56 | 168 | 96 | 1.77 |
| ErTlSe ₂ | 570117 | 111 | rhomb. | <i>R3m</i> | 2.58 | 169 | 96 | 1.40 |
| Ba ₂ NCl | 1018099 | 111 | rhomb. | <i>R3m</i> | 2.64 | 174 | 93 | 1.28 |
| Ba(MgP) ₂ | 8278 | 001 | hex. | <i>P3m1</i> | 2.67 | 176 | 92 | 1.13 |
| NaDySe ₂ | 999488 | 111 | rhomb. | <i>R3m</i> | 2.73 | 180 | 90 | 1.92 |
| Sr ₂ BBrN ₂ | 1077553 | 111 | rhomb. | <i>R3m</i> | 2.81 | 185 | 88 | 2.45 |
| SrF ₂ | 981 | 111 | cubic | <i>Fm3m</i> | 2.84 | 187 | 87 | 6.78 |

TABLE IV. Additional thermodynamically stable systems for a wider range of V_1^* than reported in Table II in the main text.

| Composition | mp-id | Surface | Lattice | SG | $ \epsilon \%$ | V_1^* (meV) | Moiré length (nm) | Gap (eV) | E_{hull} (meV) |
|----------------------------------|---------|---------|---------|------------|----------------|---------------|-------------------|----------|-------------------------|
| CuI | 22895 | 111 | cubic | $F43m$ | 0.16 | 11 | 150.13 | 1.18 | 6.76 |
| NaBH ₄ | 976181 | 111 | cubic | $F43m$ | 0.29 | 19 | 86.15 | 6.59 | 11.45 |
| CsPrS ₂ | 9080 | 111 | rhomb. | $R3m$ | 0.30 | 20 | 81.98 | 2.26 | 1.41 |
| LiI | 22899 | 111 | cubic | $Fm3m$ | 0.32 | 21 | 76.05 | 4.24 | 36.53 |
| CuI | 569346 | 001 | hex. | $P6_3mc$ | 0.37 | 25 | 66.01 | 1.21 | 9.15 |
| CsNdS ₂ | 9081 | 111 | rhomb. | $R3m$ | 0.46 | 30 | 54.02 | 2.25 | 1.53 |
| MgSe | 1018040 | 001 | hex. | $P6_3mc$ | 0.49 | 32 | 50.74 | 2.58 | 42.17 |
| Sr ₂ H ₃ I | 1019269 | 001 | hex. | $P3m1$ | 0.61 | 40 | 40.17 | 2.15 | 8.07 |
| LiI | 568273 | 001 | hex. | $P6_3/mmc$ | 0.69 | 45 | 35.93 | 4.24 | 33.21 |
| PbS | 1057015 | 111 | rhomb. | $R3m$ | 0.70 | 46 | 35.47 | 1.04 | 1.34 |
| CdI ₂ | 570437 | 001 | hex. | $P3m1$ | 1.30 | 86 | 18.95 | 2.40 | 1.25 |
| CdI ₂ | 568289 | 111 | rhomb. | $R3m$ | 1.34 | 88 | 18.47 | 2.38 | 8.45 |
| CdI ₂ | 567296 | 001 | hex. | $P3m1$ | 1.34 | 88 | 18.44 | 2.38 | 1.52 |
| KLiS | 1077266 | 001 | hex. | $P6_3/mmc$ | 1.35 | 89 | 18.30 | 2.74 | 48.94 |
| CdI ₂ | 28248 | 001 | hex. | $P6_3mc$ | 1.40 | 92 | 17.67 | 2.44 | 0.62 |
| CdI ₂ | 567259 | 001 | hex. | $P3m1$ | 1.67 | 110 | 14.75 | 2.40 | 1.79 |
| CdS | 2469 | 111 | cubic | $F43m$ | 1.69 | 111 | 14.64 | 1.05 | 1.46 |
| ScP | 1009746 | 111 | cubic | $F43m$ | 1.79 | 117 | 13.82 | 1.68 | 530.03 |
| LaF ₃ | 8354 | 001 | hex. | $P6_3/mmc$ | 1.86 | 122 | 13.24 | 5.74 | 19.58 |
| AgI | 22919 | 111 | cubic | $Fm3m$ | 2.02 | 133 | 12.20 | 1.01 | 92.18 |
| ZnTe | 8884 | 001 | hex. | $P6_3mc$ | 2.10 | 138 | 11.75 | 1.10 | 5.24 |
| NaH | 1009220 | 111 | cubic | $Pm3m$ | 2.16 | 142 | 11.41 | 1.50 | 157.43 |
| ZnTe* | 571195 | 001 | hex. | $P3_1$ | 2.26 | 149 | 10.90 | 1.07 | 3.69 |
| GeI ₂ | 567677 | 001 | hex. | $P6m2$ | 2.55 | 168 | 9.68 | 2.17 | 150.90 |
| SrF ₂ | 1019258 | 001 | hex. | $P6_3/mmc$ | 2.76 | 181 | 8.94 | 5.94 | 170.96 |

TABLE V. Candidate substrates with formation energies above the convex hull of the Gibbs free energy. While in principle they can be thermodynamically unstable, they may form long lived metastable states. Formation energies above the convex hull are given in the far right column. The * on ZnTe in the $P3_1$ phase indicates that this is the only substrate without mirror symmetry.